NACA

RESEARCH MEMORANDUM

SUPERSONIC AERODYNAMIC CHARACTERISTICS OF

A LOW-DRAG AIRCRAFT CONFIGURATION HAVING AN ARROW

WING OF ASPECT RATIO 1.86 AND A BODY OF

FINENESS RATIO 20

By Warren Gillespie, Jr.

Langley Aeronautical Laboratory
Langley Field, Va.

NATIONAL ADVISORY COMMITTEE
FOR AERONAUTICS
WASHINGTON
March 19, 1957

B

CONFIDENTIAL

NATIONAL ADVISORY COMMITTEE FOR AERONAUTICS

RESEARCH MEMORANDUM

SUPERSONIC AERODYNAMIC CHARACTERISTICS OF

A LOW-DRAG AIRCRAFT CONFIGURATION HAVING AN ARROW

WING OF ASPECT RATIO 1.86 AND A BODY OF

FINENESS RATIO 20

By Warren Gillespie, Jr.

SUMMARY

A free-flight rocket-propelled model investigation was conducted at Mach numbers of 1.2 to 1.9 to determine the longitudinal and lateral aerodynamic characteristics of a low-drag aircraft configuration. The model consisted of an aspect-ratio-1.86 arrow wing with 67.5° leading-edge sweep and NACA 65A004 airfoil section, and a triangular vertical tail with 60° sweep and NACA 65A003 section, in combination with a body of fineness ratio 20. Aerodynamic data in pitch, yaw, and roll were obtained from transient motions induced by small pulse rockets firing at intervals in the pitch and yaw directions.

From the results of this brief aerodynamic investigation, it is observed that very slender body shapes can provide increased volumetric capacity with little or no increase in zero-lift drag, and that body fineness ratios of the order of 20 should be considered in the design of long-range supersonic aircraft. The zero-lift drag and the drag-due-to-lift parameter of the test configuration varied linearly with Mach number. The maximum lift-drag ratio was 7.0 at a Mach number of 1.25 and decreased slightly to a value of 6.6 at a Mach number of 1.81. The optimum lift coefficient, normal-force-curve slope, lateral-force-curve slope, static stability in pitch and yaw, time to damp to one-half amplitude in pitch and yaw, the sum of the rotary damping derivatives in pitch and also in yaw, and the static rolling derivatives all decreased with an increase in Mach number.

Values of certain rolling derivatives were obtained by application of the least-squares method to the differential equation of rolling motion. A comparison of the experimental and calculated total rolling-moment-coefficient variation during transient oscillations of the model indicated good agreement when the damping-in-roll contribution was included with the static rolling-moment terms.

CONFIDENTIAL

INTRODUCTION

Several methods have been developed whereby the drag of aircraft configurations can be reduced at supersonic speeds. (See refs. 1 to 6, for example.) In general, these methods require either the indentation and special contouring of the body in the region of the wing or the application of twist and camber to the wing. It may be well to consider a simpler approach to the problem of obtaining a low-drag aircraft configuration suitable for flight at supersonic speeds. For example, contemporary high-speed airplanes have body fineness ratios of the order of 8. The investigation of reference 7 reported in 1951 showed that parabolic bodies of fineness ratios 9 to 18 had approximately equal drag at low supersonic speeds. However, when based on volume to the two-thirds power instead of the usual area reference, the drag coefficient at a Mach number of 1.4 for the parabolic bodies was shown to decrease as the fineness ratio increased to 25.

For the present test a body of fineness ratio 20 was combined with a 4-percent-thick arrow wing of aspect ratio 1.86. The body was made cylindrical in the region of the wing and the overall axial progression of total cross-sectional area was moderate. The use of body indentation as such was avoided. The purpose of the test was to determine the aerodynamic characteristics of the resulting slender configuration at supersonic speeds and at lifting conditions. The model was flight-tested at the Langley Pilotless Aircraft Research Station at Wallops Island, Va.

SYMBOLS

C_N normal-force coefficient, $\dfrac{a_n}{g}\dfrac{W/S}{q}$

C_Y side-force coefficient, $\dfrac{a_y}{g}\dfrac{W/S}{q}$

C_X axial-force coefficient, $\dfrac{a_x}{g}\dfrac{W/S}{q}$

C_L lift coefficient, $C_N \cos \alpha + C_X \sin \alpha$

C_D drag coefficient, $-C_X \cos \alpha + C_N \sin \alpha$

C_{D_0} minimum drag coefficient (at $C_L = 0$), $-C_X$ at $C_L = 0$

L/D $\qquad$ lift-drag ratio

C_m $\qquad$ pitching-moment coefficient about center of gravity

C_n $\qquad$ yawing-moment coefficient about center of gravity based on wing area and span

C_l $\qquad$ rolling-moment coefficient about body center line

$$C_{N_\alpha} = \left(\frac{\partial C_N}{\partial \alpha}\right)_{C_N=0}$$

$C_{m_{C_N}}$ $\qquad$ static stability parameter in pitch, $\left(\dfrac{\partial C_m}{\partial C_N}\right)_{C_N=0}$

$$C_{Y_\beta} = \left(\frac{\partial C_Y}{\partial \beta}\right)_{C_Y=0}$$

$C_{n_{C_Y}}$ $\qquad$ static stability parameter in yaw, $\left(\dfrac{\partial C_n}{\partial C_Y}\right)_{C_Y=0}$

$\left(C_{m_q} + C_{m_{\dot\alpha}}\right)$ $\qquad$ sum of rotary damping derivatives in pitch,
$$C_{m_q} = \frac{\partial C_m}{\partial \frac{\dot\theta \bar c}{2V}} \quad \text{and} \quad C_{m_{\dot\alpha}} = \frac{\partial C_m}{\partial \frac{\dot\alpha \bar c}{2V}}$$

$\left(C_{n_r} - C_{n_{\dot\beta}}\right)$ $\qquad$ sum of rotary damping derivatives in yaw,
$$C_{n_r} = \frac{\partial C_n}{\partial \frac{rb}{2V}} \quad \text{and} \quad C_{n_{\dot\beta}} = \frac{\partial C_n}{\partial \frac{\dot\beta b}{2V}}$$

$T_{1/2}$ $\qquad$ time for a transient oscillation to damp to one-half amplitude, sec

P $\qquad$ period of oscillations, sec

$$C_{l_\beta} = \frac{\partial C_l}{\partial \beta}$$

$$C_{l_{\beta,\alpha}} = \frac{\partial C_{l_\beta}}{\partial \alpha}$$

$$C_{l_p} = \frac{\partial C_l}{\partial \frac{pb}{2V}}$$

$$C_{l_r} = \frac{\partial C_l}{\partial \frac{rb}{2V}}$$

$$C_{l_{\dot\beta}} = \frac{\partial C_l}{\partial \frac{\dot\beta b}{2V}}$$

a_n, a_y, a_x normal, lateral, and axial accelerations, respectively, ft/sec^2

g acceleration due to gravity, 32.2 ft/sec^2

q dynamic pressure, lb/sq ft

V velocity, ft/sec

M Mach number

R Reynolds number based on a length of 1 foot

W weight of model, 111.1 lb

α angle of attack at model center of gravity, deg

$\dot\alpha$ rate of change of angle of attack, radians/sec

β angle of sideslip at model center of gravity, deg

$\dot\beta$ rate of change of angle of sideslip, radians/sec

$\dot\gamma$ rate of change of flight-path angle, radians/sec

ϕ angle of roll, deg

$p, \dot\phi$ rolling velocity, radians/sec

$\dot p$ rolling acceleration, radians/sec^2

θ angle of pitch, deg

$\dot\theta$ angular velocity in pitch, radians/sec

$\ddot{\theta}$ angular acceleration in pitch, radians/sec^2

ψ angle of yaw, deg

$r, \dot{\psi}$ angular velocity in yaw, radians/sec

S   total wing area to body center line, 4.31 sq ft

c   local wing chord

$\bar{c}$ wing mean aerodynamic chord, 2.03 ft

b   wing span, 2.83 ft

x'   chordwise distance back from leading edge of local chord

y   spanwise distance of local chord out from body center line

I_Y moment of inertia in pitch about center of gravity, 12.2 slug-ft^2

I_Z moment of inertia in yaw about center of gravity, 12.3 slug-ft^2

I_X moment of inertia in roll about model center line, 0.314 slug-ft^2

I_{XZ} product of inertia, assumed equal to zero

The positive directions of the angles and coefficients are shown in figure 1.

MODEL

A drawing of the model is shown in figure 2 and photographs of the model are presented in figures 3 and 4. The fuselage ordinates are listed in table I, and physical characteristics of the model are listed in table II. The configuration for this test consisted essentially of an arrow wing of aspect ratio 1.86 with 67.5° leading-edge sweep and NACA 65A004 airfoil section attached at body-center-line height to the cylindrical midsection of a slender body of fineness ratio 20. The model was somewhat similar to the large body configuration, model 5 of reference 8. A triangular vertical tail with 60° leading-edge sweep and NACA 65A003 airfoil section provided directional stability. The tail was mounted on top of the body to simulate an airplane configuration. The ratio of fuselage frontal area to wing plan-form area was 0.032.

The angle of incidence of the wing with respect to the body center line
was zero. The wing dihedral was also zero.

The model was of metal construction with a solid aluminum-alloy
wing. Six pulse rockets were carried within the forward and rearward
fuselage sections, with four firing in the pitch direction and two in
the yaw direction. The model also carried an eight-channel telemeter
with angle-of-attack angle-of-sideslip, accelerometer, and rate-of-roll
instruments. The model was externally boosted by two Deacon rockets.
An underslung adapter was used to couple the model and booster. A sup-
port fitting, shown in figure 2, extended below the fuselage and remained
with the model.

TEST

A wing panel and the vertical tail were statically tested to meas-
ure the streamwise wing twist due to loading concentrated along the
50-percent-chord line. The flexibility of these model components is
presented in figures 5 to 7.

The model was flight tested at Mach numbers from 1.2 to 1.9 at the
Langley Pilotless Aircraft Research Station at Wallops Island, Va. Data
were obtained during ascent of the model after separation from the booster.
A smoke trail of short duration was generated from a chemical solution con-
tained in the end of the model which aided in tracking the flight. Aero-
dynamic data in pitch, yaw, and roll were obtained from transient oscil-
lating motions induced by pulse rockets firing at intervals in the pitch
and yaw directions. The telemeter system permitted the measurement of
angles of attack and sideslip; normal, lateral, and longitudinal accelera-
tions; angular accelerations in pitch and roll; and rolling velocity. The
velocity obtained from a CW Doppler radar set (corrected for wind velocity)
was used in conjunction with tracking radar and radiosonde data to calcu-
late Mach number, Reynolds number, and dynamic pressure. The variations
of the free-stream Reynolds number per foot of length and dynamic pressure
with Mach number are shown in figure 8. Variations of the angle of attack
with induced sideslip angle caused by pitch pulses are shown in figure 9.
Likewise, the variations of the induced angle of attack with sideslip
angle caused by yaw pulses are shown in figure 10. The variations are
for the maximum oscillations obtained after a pulse.

ACCURACY AND CORRECTIONS

Errors in the absolute value of a telemetered quantity are thought
to be within ±1 percent of the range of the instrument. At a Mach number

of 1.5 the resulting errors in the normal-, lateral-, and axial-force coefficients have been calculated to be within ±0.01, ±0.001, and ±0.001, respectively. Mach number is estimated to be accurate within ±1 percent and dynamic pressure within ±2 percent. Experience in the use of the air-flow indicator shows that an error of ±0.3° is probable.

In order to avoid error, in the determination of the drag polars, that could result from either external or internal misalinement of the longitudinal (axial) accelerometer instrument when subjected to normal acceleration, the angularity of the mounting base in the model was measured. The instrument itself was calibrated while subjected to normal acceleration. The base of the accelerometer was ground to reduce the response of the instrument to normal-force interaction. The residual internal instrument error due to normal acceleration and the external misalinement of the instrument mounting base were accounted for in the data reduction.

An additional source of inaccuracy in the final results may be the induced lateral motions following a pitch pulse or the induced pitch motions following a yaw pulse. The relative magnitude of the induced lateral motions to pitch motions increased with an increase in Mach number. However, cross-coupling effects on the data presented are believed to be small.

Measurements obtained from the flow indicator were corrected for pitching and yawing velocities and for flight-path curvature. Position corrections were made to measurements obtained from the normal, lateral, and longitudinal accelerometers mounted near the center of gravity of the model.

ANALYSIS

The instantaneous pitching moment was measured by means of an angular accelerometer. The pitching moment due to angle of attack is given by the following expression:

$$C_m(\alpha) = \frac{I_Y \ddot{\theta}}{qS\bar{c}} - \left(C_{m_q} + C_{m_{\dot{\alpha}}}\right)\dot{\alpha} - C_{m_q}\dot{\gamma}$$

However, for the present test the rotary-damping terms were negligible, and the pitching moment due to angle of attack was calculated by the following simplified expression:

$$C_m(\alpha) = \frac{I_Y \ddot{\theta}}{qS\bar{c}}$$

The oscillations in pitch resulting from the pitch-pulse rockets have been analyzed assuming two degrees of freedom. A similar analysis was made for the oscillations in yaw caused by the yaw-pulse rockets. Values of C_{m_α} and C_{n_β} were calculated using the following expressions:

$$C_{m_\alpha} = - \frac{\left[\left(\frac{2\pi}{P}\right)^2 + \left(\frac{0.693}{T_{1/2}}\right)^2\right] I_Y}{57.3 q S \bar{c}}$$

$$C_{n_\beta} = \frac{\left[\left(\frac{2\pi}{P}\right)^2 + \left(\frac{0.693}{T_{1/2}}\right)^2\right] I_Z}{57.3 q S b}$$

These values were divided by corresponding values of C_{N_α} and C_{Y_β} to obtain the static stability parameters $C_{m_{C_N}}$ and $C_{n_{C_Y}}$. Rotary damping derivatives were calculated as follows:

$$\left(C_{m_q} + C_{m_{\dot{\alpha}}}\right) = \frac{2V}{\bar{c}^2}\left[\frac{C_{N_\alpha}}{57.3 \frac{W}{g} V} - \frac{2\left(\frac{0.693}{T_{1/2}}\right)}{q S}\right] I_Y$$

$$\left(C_{n_r} - C_{n_{\dot{\beta}}}\right) = \frac{2V}{b^2}\left[\frac{-C_{Y_\beta}}{57.3 \frac{W}{g} V} - \frac{2\left(\frac{0.693}{T_{1/2}}\right)}{q S}\right] I_Z$$

The instantaneous rolling moment was also measured by means of an angular accelerometer. Rolling-moment derivatives were obtained by application of the method of least squares to the differential equation of rolling motion. Determination of the rolling-moment derivatives is explained in the appendix.

RESULTS AND DISCUSSION

The aerodynamic test results are presented in figures 11 to 25 for a configuration having a wing and a vertical tail with flexibility characteristics that could be representative of a typical aircraft in this speed range. No aeroelastic corrections have been made to the measured data obtained during free-flight of the model.

Trim

Figure 11 presents the trim measurements for the model. Because the model was not perfectly symmetrical or because of measurement inaccuracies, the trim values for angle of attack, normal-force coefficient, angle of sideslip, rolling velocity, and lateral-force coefficient are slightly different from zero. The trim angle of attack and normal-force coefficient were constant with change in Mach number. The trim angle of sideslip, rolling velocity, and lateral-force coefficient all decreased with increasing Mach number.

Drag

Drag polars were obtained at Mach numbers of 1.25, 1.46, 1.69, and 1.81 and are shown in figure 12. Plots of normal-force coefficient against axial-force coefficient are plotted also. The data indicate a reduction in axial-force coefficient with increase in normal-force coefficient. This reduction may be due in part to some suction on the highly swept leading edge of the wing, and also to less unfavorable interference from the wake of the flow indicator which probably induces a turbulent boundary layer well forward on the body of the model, particularly at zero angle of attack. In this connection the results of references 9 and 10 show that the drag at zero lift of a 60° delta-wing—body configuration (of similar size to the present test model) was 12 to 16 percent higher with an air-flow indicator.

The drag coefficient at zero lift is plotted against Mach number in figure 13(a) and is seen to decrease linearly with increase in Mach number. A comparison is made with the large body configuration, model 5, of reference 8 which had the same wing plan form and maximum wing thickness and almost the same ratio of body maximum cross-sectional area to wing area. The body fineness ratio was 14.9, however, compared with 20 for the present model. The drag at zero lift of the two models is almost the same. The present test model has a considerably larger ratio of $\dfrac{(\text{Fuselage volume})^{2/3}}{\text{Wing area}}$ than the model of reference 8. The value of this ratio (hereinafter called the relative fuselage volume) is 0.202 for the present test model and 0.148 for the reference model. This drag comparison is somewhat surprising in view of the fact that the present model was not aerodynamically "clean" inasmuch as it had six pulse-rocket holes in the fuselage in addition to a sting-mounted flow indicator.

The larger 60° delta-wing—body configuration (model 4 of ref. 9) had very nearly the same ratio of body maximum cross-sectional area to wing area as the present test model. A direct comparison of the zero-lift drag of these two models is made in figure 13(a) and indicates slightly lower drag for the larger size model of reference 9. However,

~~Aut letessaiut~~

if allowance is made for the higher test Reynolds number of model 4 of reference 9 and the relative "cleanness" of these two models, then the present test model is indicated to have approximately the same drag. References 8 and 9 further indicate that the wing-with-interference drag of these two models is also approximately equal. The relative fuselage volume for the model of this test is, of course, much larger, being 0.202 for the present model but only 0.113 for model 4 of reference 9. It is observed, on the basis of the foregoing comparisons at zero lift, that very slender body shapes can provide increased volumetric capacity with little or no increase in drag.

The variation of the drag-due-to-lift parameter dC_D/dC_L^2 with Mach number is linear. (See fig. 13(b).) This wing plan form is not an optimum one, particularly at low supersonic speeds. Comparison with the 60° delta-wing model of reference 10 shows lower drag-due-to-lift values for that model. However, at a Mach number of 1.6 the drag-due-to-lift parameter of the present model is only 4 percent higher and probably would be equal at a Mach number of 1.7.

As a consequence of the linearity of both the variation of the zero-lift drag and the variation of the drag-due-to-lift parameter with Mach number, the drag of the test model at lift can be represented with good accuracy over the test range of Mach number by an expression of the following form:

$$C_D = \left[\left(C_{D_0} \right)_{M=1.25} - \frac{dC_{D_0}}{dM}(M - 1.25) \right] + \left[\left(\frac{dC_D}{dC_L^2} \right)_{M=1.25} + \frac{d\left(\frac{dC_D}{dC_L^2} \right)}{dM}(M - 1.25) \right] C_L^2$$

Such an expression might be of value in simplifying the preliminary performance calculations encountered in the determination of an optimum supersonic aircraft with the restriction that the configuration be not too far different from that of the present test model for which this result is specifically applicable.

Lift-Drag Ratio

Figure 14 presents the variation of lift-drag ratio with lift coefficient obtained at Mach numbers of 1.25, 1.46, 1.69, and 1.81. The dashed-line extensions of the plots at the two higher Mach numbers were obtained using the expression $C_D = C_{D_0} + \left(dC_D/dC_L^2 \right) C_L^2$ and figure 13.

The points were plotted using both positive and negative regions of the lift-drag data. Maximum lift-drag ratios of 7.0 to 6.6 are indicated to occur at an optimum lift coefficient of approximately 0.2. The variations

of maximum lift-drag ratio and optimum lift coefficient with Mach number
are shown in figure 15. Both quantities decrease nearly linearly with
increasing Mach number.

The maximum lift-drag ratio of the present model compares favorably
with the results obtained for the aspect-ratio-3.5 swept-wing airplane
configuration of references 11 and 12. This referenced configuration had
very nearly the same ratio of maximum body cross-sectional area to wing
area as the present model, and like the present model had a cylindrical
fuselage in the region of the wing intersection. The relative fuselage
volume is less, however, being 0.15 for the fineness-ratio-14.3 fuselage
of reference 11. It can therefore be stated that body fineness ratios of
the order of 20 should be considered in the design of long-range supersonic
aircraft.

Normal Force and Pitching Moment

Figures 16 to 18 present plots of normal-force and pitching-moment
coefficients and summarize the variations of the normal-force-curve and
pitching-moment-curve slopes with Mach number. Figure 16 shows that the
variation of normal-force coefficient with angle of attack is essentially
linear for small angles of attack. However, the data for a Mach number
of 1.25 show that the slope of the curve $\left(C_{N_\alpha}\right)$ increases at the higher
values of C_N and α. The data for Mach numbers of 1.46, 1.69, and 1.81
do not extend far enough in the C_N and α ranges to indicate whether a
similar increase in C_{N_α} occurs. However, the force data of reference 13
for a $68.4°$ delta wing show that an essentially linear variation would be
expected at a Mach number of 1.9 up to an angle of attack of about $8°$
where the slope should begin to decrease because of separation effects.
The variation of normal-force coefficient with pitching-moment coeffi-
cient presented in figure 17 is approximately linear over the range of
the test conditions. The variation of the normal-force-curve slope C_{N_α}
with Mach number shown in figure 18(a) is linear and decreases from a
value of 0.041 at a Mach number of 1.25 to 0.033 at a Mach number of 1.81.
Experimental values of C_{N_α} are approximately 5 percent lower than the
values obtained when using the theoretical method of reference 14. This
comparison indicates very little probable loss in C_{N_α} due to wing
flexibility. A rough estimate based on the aeroelastic analysis of the
3-percent-thick, $60°$ delta wing used on the model of reference 10 gives
a probable reduction of C_{N_α} from rigid-wing values of only 4 percent.
Consequently, a more detailed aeroelastic analysis has not been made for
the present test model, since the effects of aeroelasticity are probably
small.

The variation of the static stability parameter $C_{m_{C_N}}$ with Mach number is shown in figure 18(b). The experimental results obtained by two methods are in close agreement. It is indicated by this agreement that lateral oscillations which accompanied the longitudinal motions had a negligible effect on the longitudinal period. The result calculated using the method of reference 14 compares favorably with the experimental curves, but does not show the gradual reduction in static stability as Mach number increases. This reduction noted in the tests is probably caused by greater wing aeroelasticity for conditions of increased dynamic pressure which occurred at the higher test Mach numbers.

Longitudinal Dynamic Stability

Figure 19(a) shows that the time for the pitching oscillation to damp to one-half amplitude decreased with an increase in Mach number, or that the total damping increased with Mach number. One would expect a more uniform decrease in $T_{1/2}$ with Mach number rather than the leveling-off tendency shown in the figure at the higher Mach numbers. This effect is reflected in figure 19(b) which shows negligible rotary damping in this region. The theory and experimental tests of references 10, 15, and 16 indicate that at a Mach number of 1.8 the damping derivatives $\left(C_{m_q} + C_{m_{\dot{\alpha}}}\right)$ should have a value of about -0.8 to -0.5. The slope of the curve of figure 19(b) is four times greater than the results of references 10, 15, and 16 indicate. The average value of the curve of figure 19(b) is, however, in agreement. It should be pointed out that the experimental accuracy of the damping derivatives $\left(C_{m_q} + C_{m_{\dot{\alpha}}}\right)$ is very poor, because these derivatives are obtained from the difference of two numbers having the same order of magnitude. The important point to be made is that the level of the total pitch damping for this tailless (no horizontal tail) configuration was low, being only one-third that determined for the model of reference 12 which had a horizontal tail.

Side Force and Static Directional Stability

Plots of side-force coefficient against angle of sideslip are presented in figure 20 for Mach numbers of 1.25, 1.46, 1.59, 1.69, 1.81, and 1.86. For the small range of the measurements, the variation of C_Y with β is linear. The slopes obtained from the curves of figure 20 have been used to obtain the variation of C_{Y_β} with Mach number shown in figure 21(a). The variation is approximately linear. The static stability parameter $C_{n_{C_Y}}$ obtained from periods of the yaw pulses is also plotted against Mach number in figure 21(b). Comparison with the corresponding

data of figure 18(b) indicates that the aerodynamic center in yaw was 0.2$\bar{c}$ farther rearward than the aerodynamic center in pitch.

Directional Dynamic Stability

Figure 22(a) shows that the time for the yawing oscillations to damp to one-half amplitude decreased with an increase in Mach number. The rotary yaw damping $\left(C_{n_r} - C_{n_{\dot{\beta}}}\right)$ decreased slightly with increased Mach number. (See fig. 22(b).)

Rolling-Moment Derivatives

Rolling-moment derivatives $\left(C_{l_\beta}\right.$ at zero angle of attack and C_{l_β} per degree angle of attack$\left.\right)$ were obtained by application of a least-squares method to the differential equation of rolling motion. The method is outlined in the appendix. Although the method is theoretically capable of also determining the derivatives C_{l_p} and $\left(C_{l_r} - C_{l_{\dot{\beta}}}\right)$, accurate values of these rotary derivatives could not be determined. Estimates indicate that the contributions of these terms, particularly of $\left(C_{l_r} - C_{l_{\dot{\beta}}}\right)$, are small in comparison with the contributions of the static rolling-moment derivatives $\left(C_{l_\beta}\right)_{\alpha=0}$ and $C_{l_{\beta,\alpha}}$ to the total rolling moment experienced by the model. This is a fortunate situation, and it appears that those derivatives which have a greater influence on the motion of a particular configuration will be the ones that can be more accurately evaluated by this method of data reduction.

The least-squares method is applicable irrespective of the uniformity of the lateral motions. Simultaneously occurring lateral and longitudinal (or cross-coupled) motions can be utilized for purposes of stability-derivative evaluation. The derivative C_{l_β} can be broken down to its fundamental parts, $\left(C_{l_\beta}\right)_{\alpha=0}$ and $C_{l_{\beta,\alpha}}$. Thus, the motion restrictions necessary to the proper employment of other methods such as the graphical vector method (used in refs. 17 and 18, for example) are greatly relaxed or avoided, and the stability derivatives $\left(C_{l_\beta}\right)_{\alpha=0}$ and $C_{l_{\beta,\alpha}}$ may be obtained in lieu of the single derivative C_{l_β} corresponding to some average condition of longitudinal trim.

Figure 23 presents the values of rolling-moment coefficients obtained from rolling motions of the model caused either by pitch or yaw pulses. A reduction of the absolute values with increase in Mach number is noted.

The experimental results are compared with the theoretical variations calculated by using the appropriate formulas of references 19 and 20. The agreement is seen to be generally satisfactory although the theories predict somewhat higher values in both cases. For this configuration the vertical tail was the largest contributor to $\left(C_{l_\beta}\right)_{\alpha=0}$ whereas the wing was the largest contributor to $C_{l_\beta,\alpha}$. It should be noted that the theoretical calculations did not include any interaction effects between components of the configuration tested. Apparently, such effects were small for the conditions of the present test.

Since examination of the transient motions which occurred as a result of the yaw pulses showed that amplitude ratios and phase relationships could be determined, the vector method of analysis employed in reference 18 was also used to determine values of C_{l_β}. The results of this analysis are also plotted in figure 23 where a comparison is made with the previously determined values of $\left(C_{l_\beta}\right)_{\alpha=0}$. The agreement is good, probably because the trim angle of attack was nearly zero.

The vector analysis also gave values of damping-in-roll parameter C_{l_p} of -0.12 at a Mach number of 1.59 and of -0.14 at a Mach number of 1.86. These values compare favorably with the level of values obtained by the least-squares method and also with the results reported in reference 21.

By using the values of the rolling-moment coefficients obtained from the foregoing analysis, comparisons of experimental and calculated rolling-moment-coefficient variations with sideslip angle were made. These comparisons are presented in figure 24 at Mach numbers of 1.25, 1.46, 1.69, and 1.81 for the case of the model pulsed in pitch; and in figure 25 at Mach numbers of 1.59 and 1.86 for the case of the model pulsed in yaw. The agreement is generally good when the contributions of $\left(C_{l_\beta}\right)_{\alpha=0}$, $C_{l_\beta,\alpha}$ and C_{l_p} are summed. The rolling-moment contribution of the gyroscopic reaction $\left(\text{namely, } I_Z\dot\theta\dot\psi - I_Y\dot\theta\dot\psi\right)$ was found to be negligible in the determination of the total rolling-moment coefficient C_l.

SUMMARY OF RESULTS

Results obtained from a flight test of a low-drag aircraft configuration at supersonic speeds lead to the following observations:

CONFIDENTIAL

1. Very slender body shapes can provide increased volumetric capacity with little or no increase in zero-lift drag. Body fineness ratios of the order of 20 should be considered in the design of long-range supersonic aircraft.

2. Maximum lift-drag ratios of 7.0 and 6.6 at Mach numbers of 1.25 and 1.81, respectively, were obtained.

3. The optimum lift coefficient, normal-force-curve slope, lateral-force-curve slope, static stability in pitch and in yaw, time to damp to one-half amplitude in pitch and in yaw, the sum of the rotary damping terms, and the static rolling derivatives all decreased with an increase in Mach number.

4. Comparison of the experimental and calculated variation of the total rolling-moment coefficient during transient oscillations of the model indicated good agreement when the damping-in-roll contribution was included with the static rolling-moment terms.

Langley Aeronautical Laboratory,
      National Advisory Committee for Aeronautics,
            Langley Field, Va., January 7, 1957.

APPENDIX

DETERMINATION OF ROLLING DERIVATIVES BY THE

LEAST-SQUARES METHOD

In order to utilize the transient rolling measurements obtained immediately following the pitch disturbances for the purpose of determining rolling derivatives, the least-squares method of data reduction was applied to the differential equation of rolling motion. The least-squares method is outlined in reference 22, pages 371 and 372. Data from both pitch and yaw pulses were analyzed to obtain values of the rolling derivatives.

The total net aerodynamic rolling-moment coefficient at any instant during free oscillation is given as follows:

$$C_l = \frac{I_X \dot{p} + \left(I_Z - I_Y\right)\dot{\theta}\dot{\psi} - I_{XZ}(\ddot{\psi} + p\dot{\theta})}{qSb} \qquad (1)$$

For the present model the product of inertia was assumed to be equal to zero, and the contribution of the gyroscopic reaction term was found to be negligible. The net aerodynamic rolling-moment coefficient was then obtained from the following simplified expression:

$$C_l = \frac{I_X \dot{p}}{qSb} \qquad (2)$$

This net aerodynamic coefficient was next assumed to result from a simple addition of particular rolling-moment coefficients. Thus,

$$C_l = K_1 \beta + K_2 \alpha \beta + C K_3 \dot{\psi} + C K_4 p \qquad (3)$$

where

$$K_1 = \left(C_{l_\beta}\right)_{\alpha=0}$$

$$K_2 = C_{l_{\beta,\alpha}}$$

$$K_3 = \left(C_{l_r} - C_{l_{\dot\beta}}\right)$$

$$K_4 = C_{l_p}$$

$$C = \frac{b}{2V}$$

From the telemeter, radar, and radiosonde measurements, sets of data were obtained consisting of $\dot{p}$, q, β, α, $\dot\psi$, p, and V at selected times over approximately 1 oscillation corresponding to an average Mach number. The largest amplitude oscillations immediately following a pitch or yaw pulse were used. Trim conditions for the telemetered quantities were determined, and the sets of data corrected to incremental variations from trim. The corresponding values of C_l were calculated by using equation (2). The following equations can then be written:

$$\left.\begin{aligned}
C_{l_1} &= K_1\beta_1 + K_2\alpha_1\beta_1 + C_1K_3\dot\psi_1 + C_1K_4p_1 \\
C_{l_2} &= K_1\beta_2 + K_2\alpha_2\beta_2 + C_2K_3\dot\psi_2 + C_2K_4p_2 \\
\cdot \qquad &\quad \cdot \qquad\quad \cdot \qquad\quad \cdot \qquad\quad \cdot \\
C_{l_n} &= K_1\beta_n + K_2\alpha_n\beta_n + C_nK_3\dot\psi_n + C_nK_4p_n
\end{aligned}\right\} \qquad (4)$$

The unknowns are the K's and the subscripts (the K's excepted) refer to particular sets of data. Choose as the best approximation to the unknowns those values which minimize the sum of the squares of the deviations of the observed values from the corresponding values which the observed quantity would have if computed from the chosen values of the unknowns. The following expression can then be minimized by equating to zero the four partial derivatives with respect to K_1, K_2, K_3, and K_4:

$$\sum_{j=1}^{n} \left[C_{l_j} - \left(K_1 \beta_j + K_2 \alpha_j \beta_j + C_j K_3 \dot{\psi}_j + C_j K_4 p_j \right) \right]^2 \tag{5}$$

There results the following set of equations

$$\left.\begin{aligned}
E_1 &= A_1 K_1 + B_1 K_2 + C_1 K_3 + D_1 K_4 \\
E_2 &= A_2 K_1 + B_2 K_2 + C_2 K_3 + D_2 K_4 \\
E_3 &= A_3 K_1 + B_3 K_2 + C_3 K_3 + D_3 K_4 \\
E_4 &= A_4 K_1 + B_4 K_2 + C_4 K_3 + D_4 K_4
\end{aligned}\right\} \tag{6}$$

where

$$E_1 = \sum \beta C_l \qquad A_1 = \sum \beta^2 \qquad B_1 = \sum \alpha \beta^2 \qquad C_1 = \sum C \beta \dot{\psi} \qquad D_1 = \sum C \beta p$$

$$E_2 = \sum \alpha \beta C_l \qquad A_2 = \sum \alpha \beta^2 \qquad B_2 = \sum (\alpha \beta)^2 \qquad C_2 = \sum C \alpha \beta \dot{\psi} \qquad D_2 = \sum C \alpha \beta p$$

$$E_3 = \sum C \dot{\psi} C_l \qquad A_3 = \sum C \beta \dot{\psi} \qquad B_3 = \sum C \alpha \beta \dot{\psi} \qquad C_3 = \sum (C \dot{\psi})^2 \qquad D_3 = \sum C^2 \dot{\psi} p$$

$$E_4 = \sum C p C_l \qquad A_4 = \sum C \beta p \qquad B_4 = \sum C \alpha \beta p \qquad C_4 = \sum C^2 \dot{\psi} p \qquad D_4 = \sum (C p)^2$$

Equations (6) must be solved simultaneously for the K's and the corresponding aerodynamic parameters $\left(C_{l_\beta}\right)_{\alpha=0}$, $C_{l_\beta,\alpha}$, C_{l_p}, and $\left(C_{l_r} - C_{l_{\dot{\beta}}}\right)$. The accuracy of determination of these parameters will depend on the accuracy and extent of the basic measurements and the relative importance of the various terms to the rolling motion of the configuration under consideration. In the present case values for $\left(C_{l_\beta}\right)_{\alpha=0}$ and for $C_{l_\beta,\alpha}$ were determined, but only the order of magnitude of C_{l_p} could be determined. The contribution of $\left(C_{l_r} - C_{l_{\dot{\beta}}}\right)$ was estimated to be negligible, and accurate values for the sum of these two damping derivatives could not be determined.

REFERENCES

1. Palmer, William E., Howell, Robert R., and Braslow, Albert L.:
   Transonic Investigation at Lifting Conditions of Streamline Con-
   touring in the Sweptback-Wing—Fuselage Juncture in Combination
   With the Transonic Area Rule. NACA RM L56D11a, 1956.

2. Whitcomb, Richard T.: Some Considerations Regarding the Application
   of the Supersonic Area Rule to the Design of Airplane Fuselages.
   NACA RM L56E23a, 1956.

3. Hickey, Daniel P.: Experimental Investigation of a Method of Wave-
   Drag Reduction for Combinations Employing Quasi-Cylindrical Bodies
   and Swept Wings at Supersonic Speeds. NACA RM A56I18, 1957.

4. Klunker, E. B., and Harder, Keith C.: Some Considerations of the
   Influence of Body Cross-Sectional Shape on the Lifting Efficiency
   of Wing-Body Combinations at Supersonic Speeds. NACA RM L56H30,
   1956.

5. Grant, Frederick C.: The Proper Combination of Lift Loadings for Least
   Drag on a Supersonic Wing. NACA Rep. 1275, 1956. (Supersedes NACA
   TN 3533.)

6. Willmarth, W. W.: A Survey of Existing Methods for Reducing the Drag-
   Due-to-Lift At Supersonic Speeds For Planar Systems. U. S. Air Force
   Project RAND Res. Memo. RM-1611, The RAND Corp., Dec. 30, 1955.

7. Welsh, Clement J., and deMoraes, Carlos A.: Results of Flight Tests
   To Determine Drag of Parabolic and Cone-Cylinder Bodies of Very
   Large Fineness Ratios at Supersonic Speeds. NACA RM L51E18, 1951.

8. Arbic, Richard G., and Gillespie, Warren, Jr.: Summary of Rocket-
   Model Tests at Zero Lift of an Arrow-Wing Missile Configuration From
   Mach Numbers of 0.9 to 1.8. NACA RM L53J02, 1954.

9. Morrow, John D., and Nelson, Robert L.: Large-Scale Flight Measure-
   ments of Zero-Lift Drag of 10 Wing-Body Configurations at Mach Num-
   bers from 0.8 to 1.6. NACA RM L52D18a, 1953.

10. Welsh, Clement J.: Free-Flight Investigation To Obtain Drag-at-Lift
    and Stability Data for a 60° Delta-Wing—Body Configuration Over a
    Mach Number Range of 1.3 to 1.6. NACA RM L55G14, 1955.

11. Smith, Norman J., and Hasel, Lowell E.: An Investigation at Mach Num-
    bers of 1.41 and 2.01 of the Aerodynamic Characteristics of a Swept-
    Wing Supersonic Bomber Configuration. NACA RM L52J17, 1956.

12. Chapman, Rowe, Jr.: Aerodynamic Characteristics at Mach Numbers From 0.7 to 1.75 of a Four-Engine Swept-Wing Airplane Configuration As Obtained From a Rocket-Propelled Model Test. NACA RM L55F23, 1955.

13. Hatch, John E., Jr., and Gallagher, James J.: Aerodynamic Characteristics of a 68.4° Delta Wing at Mach Numbers of 1.6 and 1.9 Over a Wide Reynolds Number Range. NACA RM L53I08, 1953.

14. Tucker, Warren A.: A Method for Estimating the Components of Lift of Wing-Body Combinations at Supersonic Speeds. NACA RM L52D22, 1952.

15. Henderson, Arthur, Jr.: Pitching-Moment Derivatives C_{m_q} and $C_{m_{\dot{\alpha}}}$ at Supersonic Speeds for a Slender-Delta-Wing and Slender-Body Combination and Approximate Solutions for Broad-Delta-Wing and Slender-Body Combinations. NACA TN 2553, 1951.

16. Tobak, Murray: Damping in Pitch of Low-Aspect-Ratio Wings at Subsonic and Supersonic Speeds. NACA RM A52L04a, 1953.

17. Wolowicz, Chester H.: Time-Vector Determined Lateral Derivatives of a Swept-Wing Fighter-Type Airplane With Three Different Vertical Tails at Mach Numbers Between 0.70 and 1.48. NACA RM H56C20, 1956.

18. Gillis, Clarence L., and Chapman, Rowe, Jr.: Effect of Wing Height and Dihedral on the Lateral Stability Characteristics at Low Lift of a 45° Swept-Wing Airplane Configuration As Obtained From Time-Vector Analyses of Rocket-Propelled-Model Flights at Mach Numbers From 0.7 to 1.3. NACA RM L56E17, 1956.

19. Bobbitt, Percy J.: Theoretical Calculations of the Lateral Stability Derivatives for Triangular Vertical Tails With Subsonic Leading Edges Traveling at Supersonic Speeds. NACA TN 3240, 1954.

20. Jones, Arthur L., Spreiter, John R., and Alksne, Alberta: The Rolling Moment Due to Sideslip of Triangular, Trapezoidal, and Related Plan Forms in Supersonic Flow. NACA TN 1700, 1948.

21. McDearman, Russell W., and Heinke, Harry S., Jr.: Investigations of the Damping in Roll of Swept and Tapered Wings at Supersonic Speeds. NACA RM L53A13, 1953.

22. Reddick, H. W., and Miller, F. H.: Advanced Mathematics for Engineers. Second ed., John Wiley & Sons, Inc., 1947.

TABLE I.- FUSELAGE ORDINATES

Station, in.	Body radius, in.
0	0
.67	.22
1.33	.38
1.67	.44
2.33	.57
3.33	.73
5.00	.98
6.67	1.19
10.00	1.54
13.33	1.82
16.67	2.06
20.00	2.23
22.75	2.35
23.33	2.37
26.67	2.45
30.00	2.50
Constant radius	Constant radius
63.38	2.50
67.43	2.45
71.49	2.37
75.54	2.23
79.60	2.06
83.65	1.82
87.71	1.54
91.76	1.19
93.79	.98
95.82	.73
97.04	.57
97.85	.44
98.25	.38
99.06	.21
99.87	0

TABLE II.- CHARACTERISTICS OF MODEL

Wing:
  Span, ft 2.83
  Area, sq ft 4.31
  Aspect ratio 1.86
  Taper ratio 0
  Sweepback of leading edge, deg 67.5
  Sweepback of trailing edge, deg 15
  Mean aerodynamic chord, $\bar{c}$, ft 2.03
  Airfoil section . . . . NACA 65A004
  Incidence, deg 0
  Dihedral, deg 0

Body:
  Maximum diameter, ft 0.42
  Length, ft 8.32
  Fineness ratio 20

Vertical tail:
  Span, ft 0.97
  Taper ratio 0
  Sweepback of leading edge, deg 60
  Sweepback of trailing edge, deg 15
  Airfoil section . . . . NACA 65A003

Model weight, lb 111.1

Moments of inertia, slug-ft^2
  In pitch 12.2
  In yaw 12.3
  In roll 0.314

Center of gravity, percent $\bar{c}$ behind leading edge of
  mean aerodynamic chord 0.197

Side view

Plan view

View forward
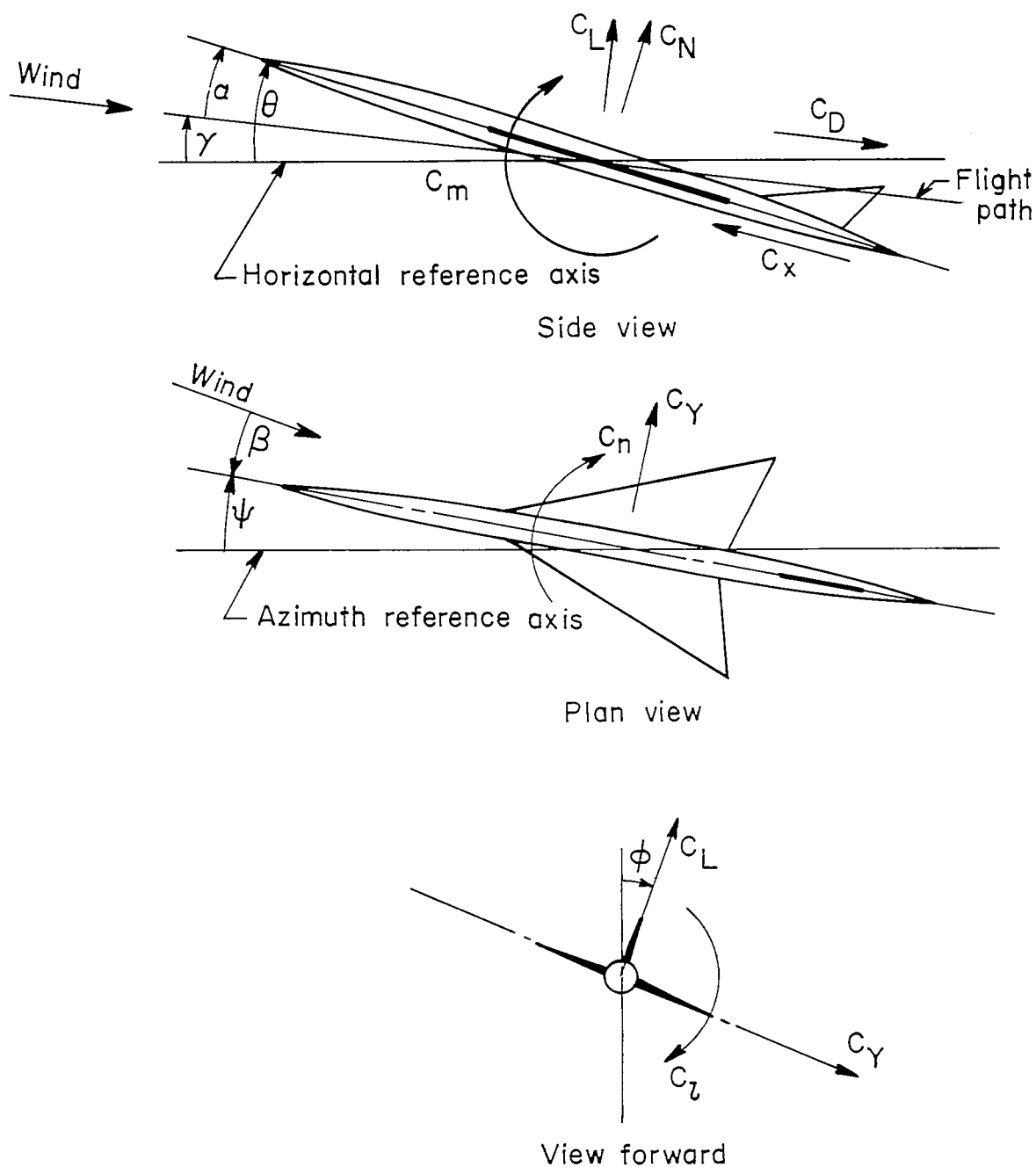
Figure 1.- System of axes. Arrows indicate positive directions; origin is at center of gravity.
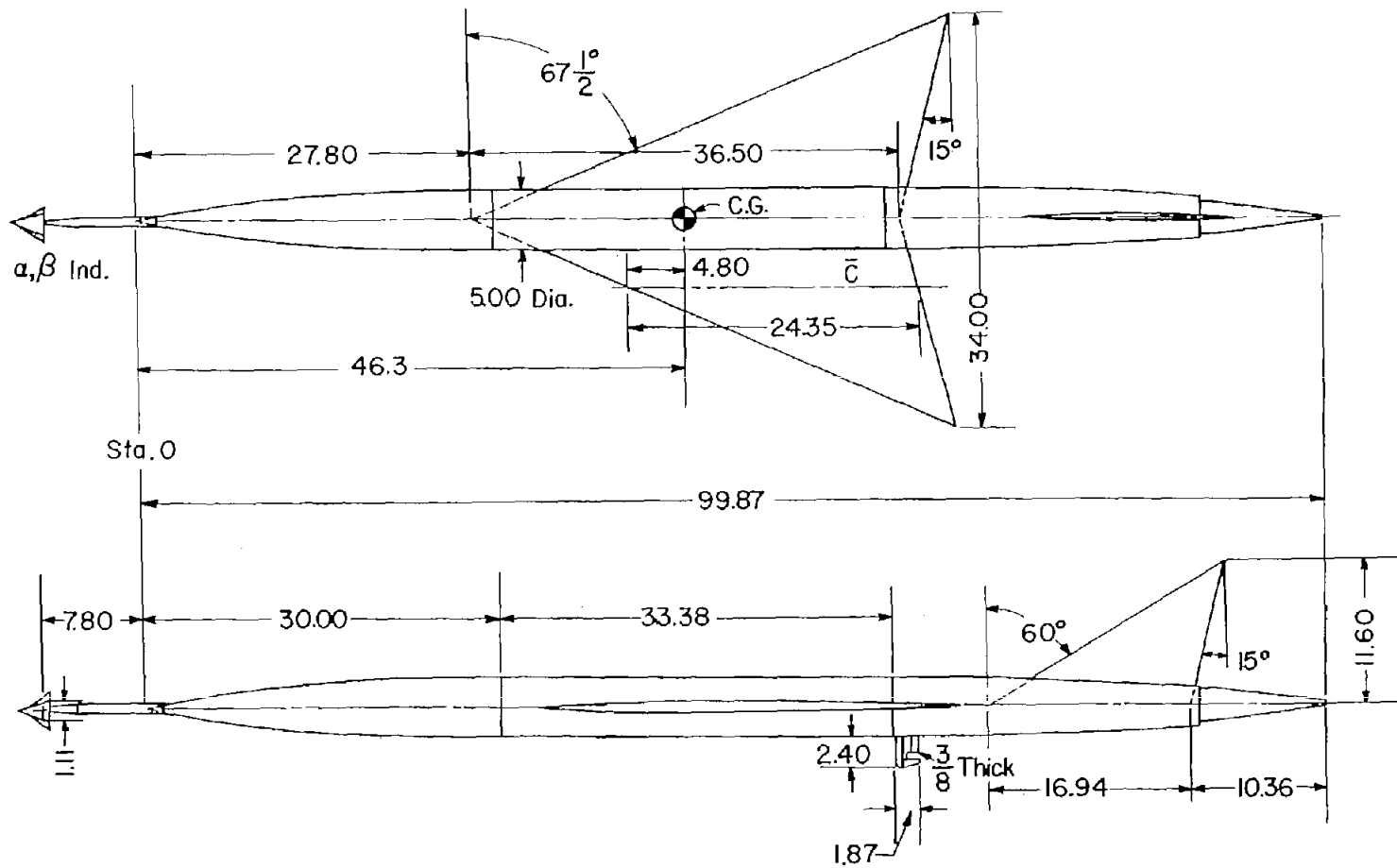
Figure 2.- Test configuration. All linear dimensions are in inches.
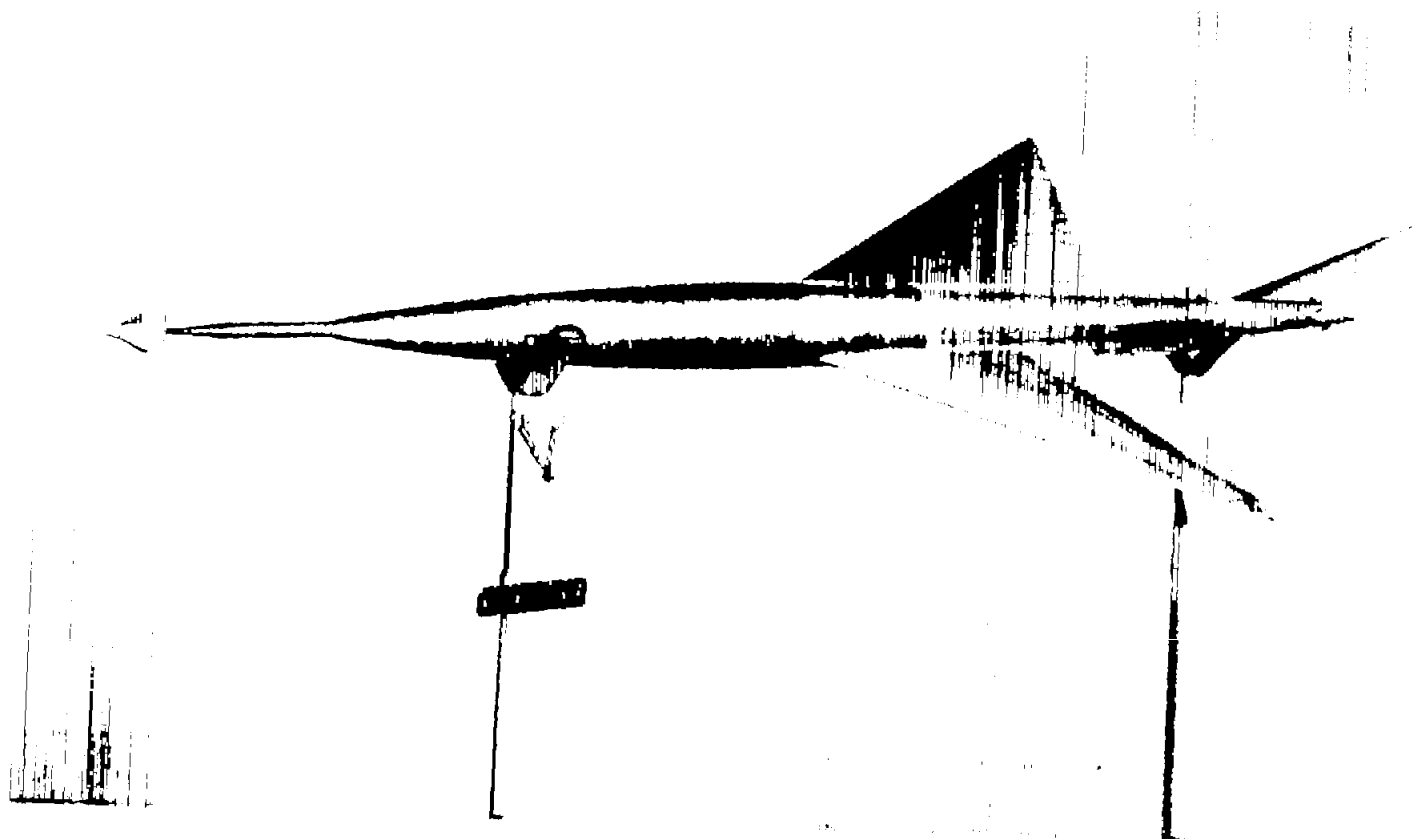
Figure 3.- Model used in investigation.   L-89979.1
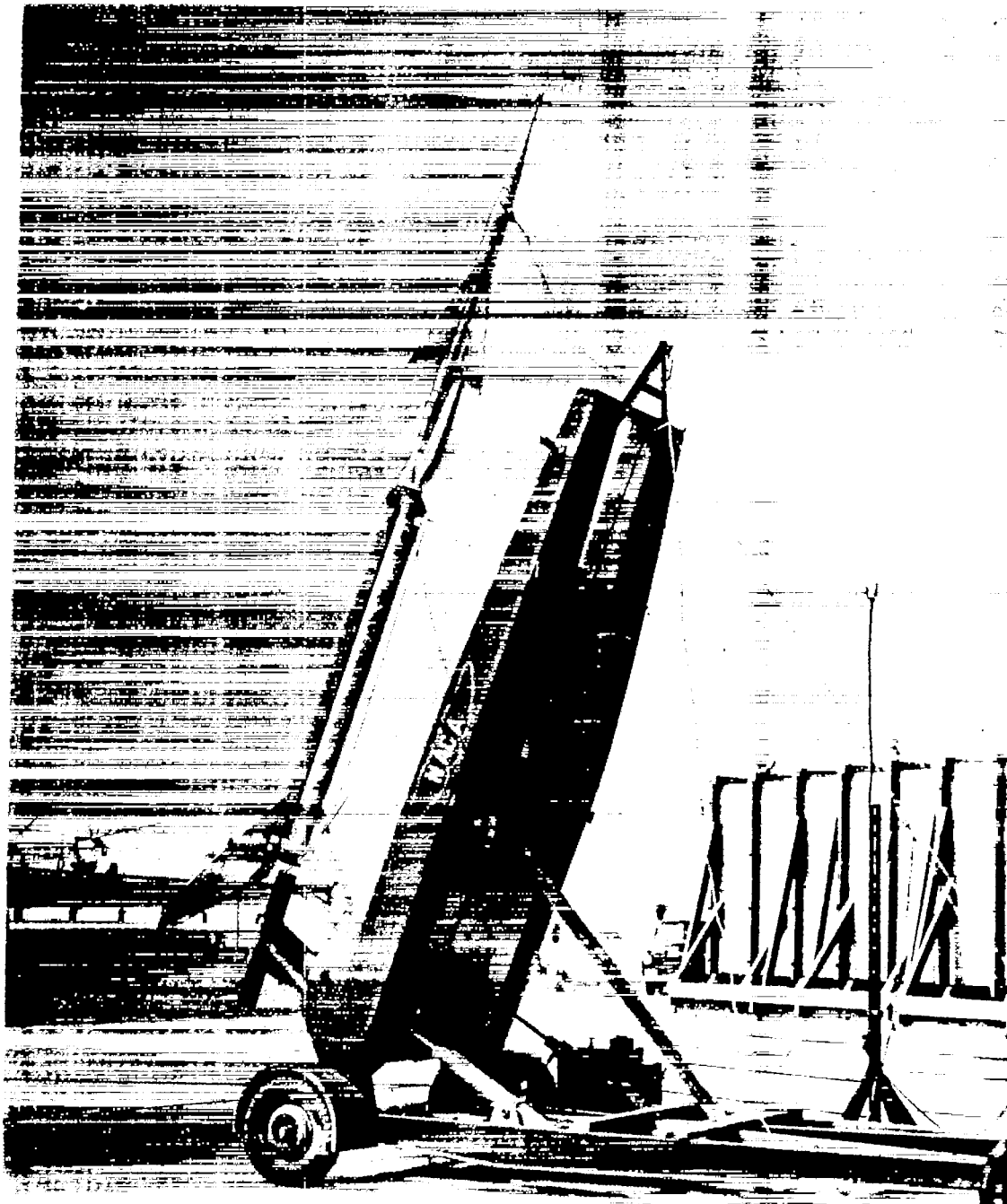
Figure 4.- Model and booster.   L-90175
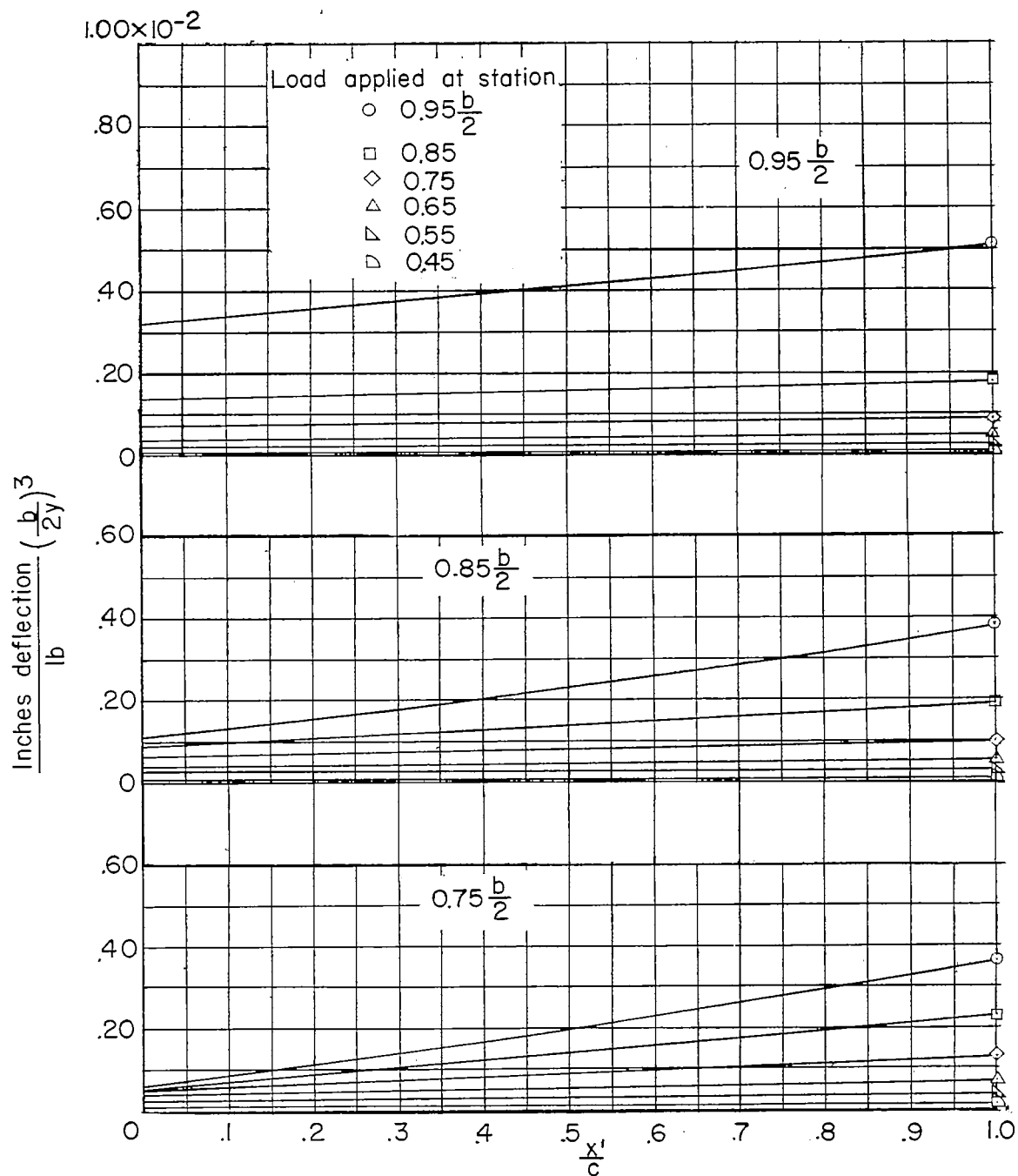
Figure 5.- Wing static deflection resulting from a concentrated load
applied along 50-percent-chord line.
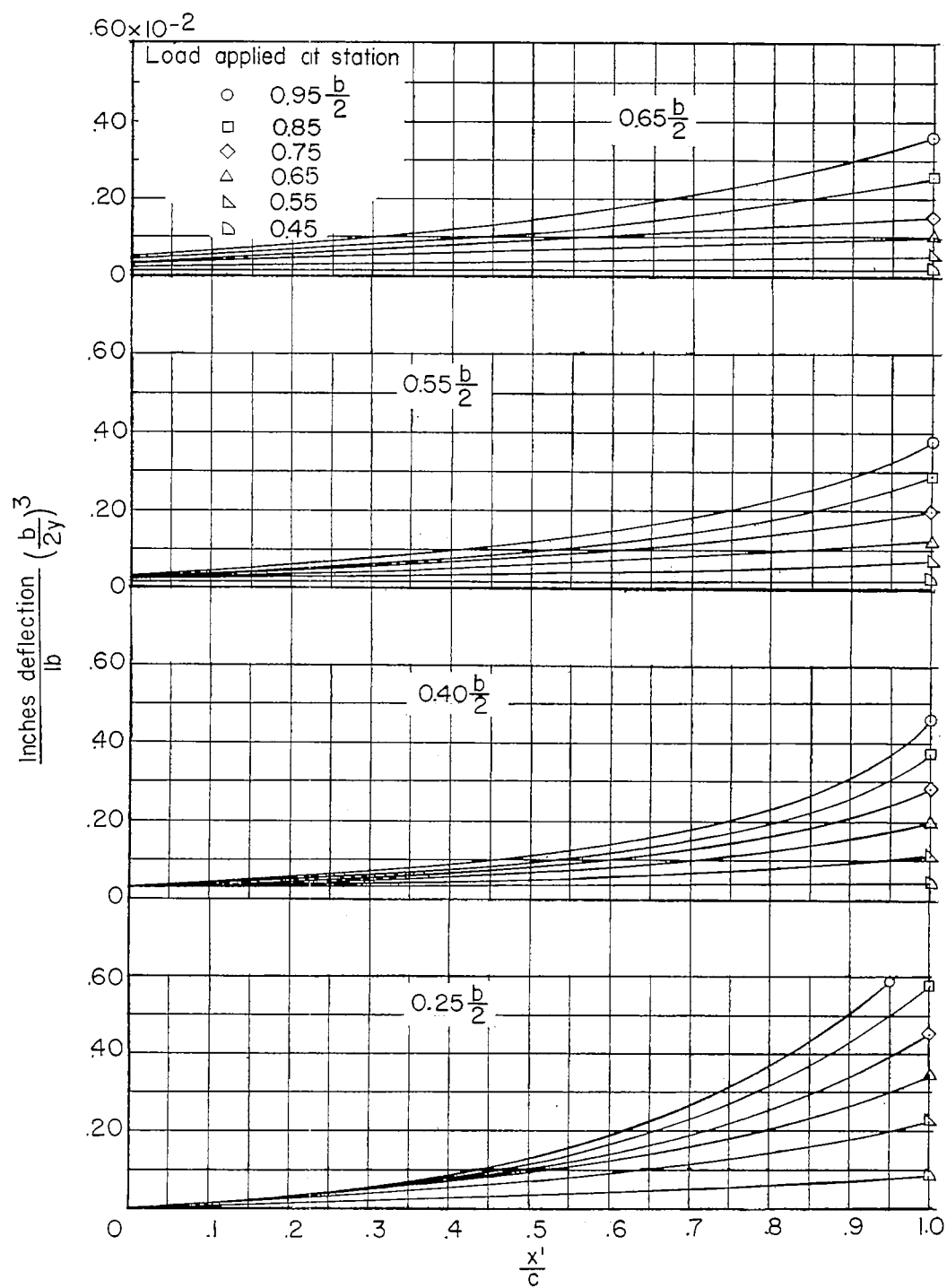
Figure 5.- Concluded.
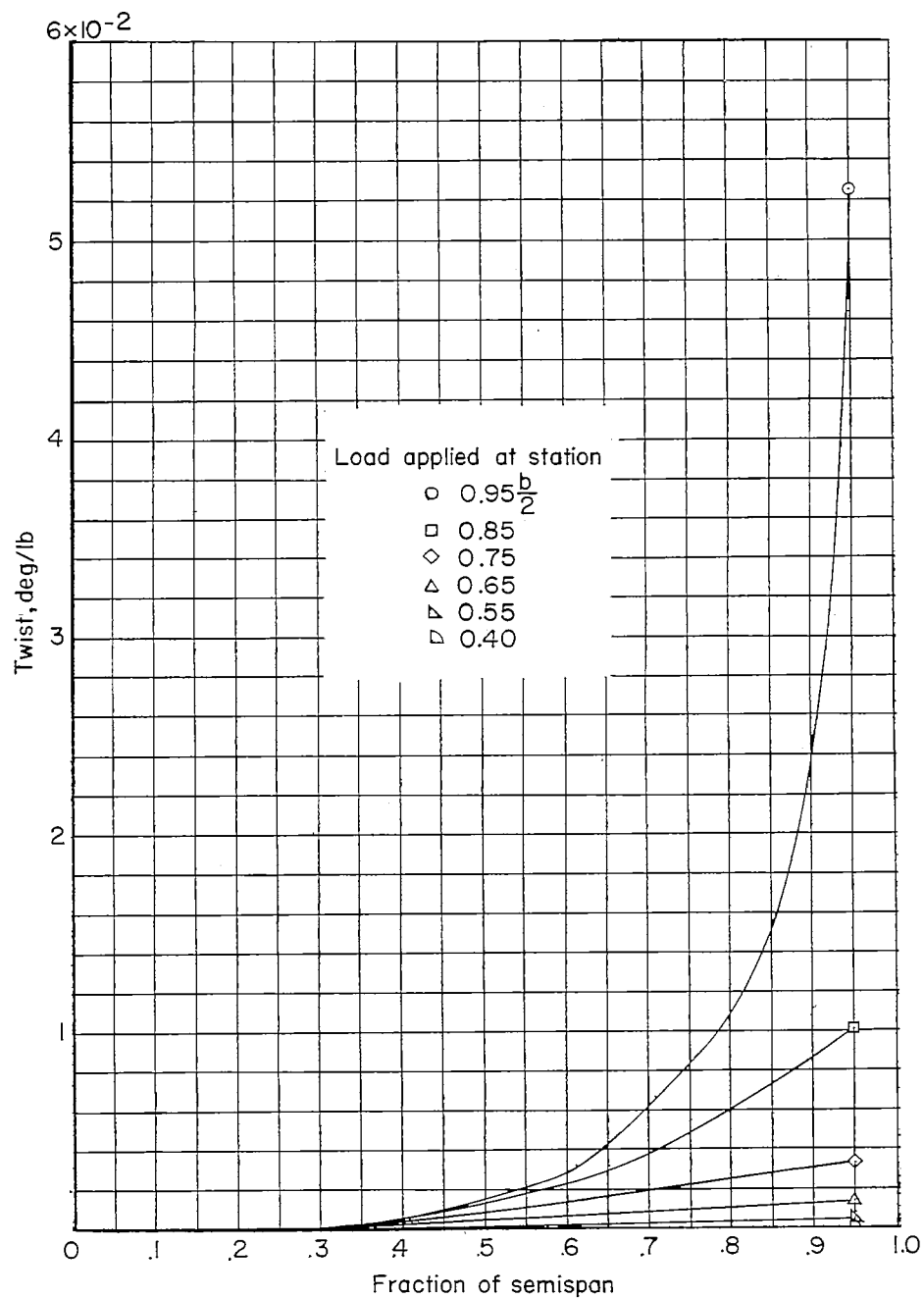
(a) Average twist from 0 to 50 percent local chord.

Figure 6.- Wing streamwise twist resulting from a concentrated load
applied along 50-percent-chord line.
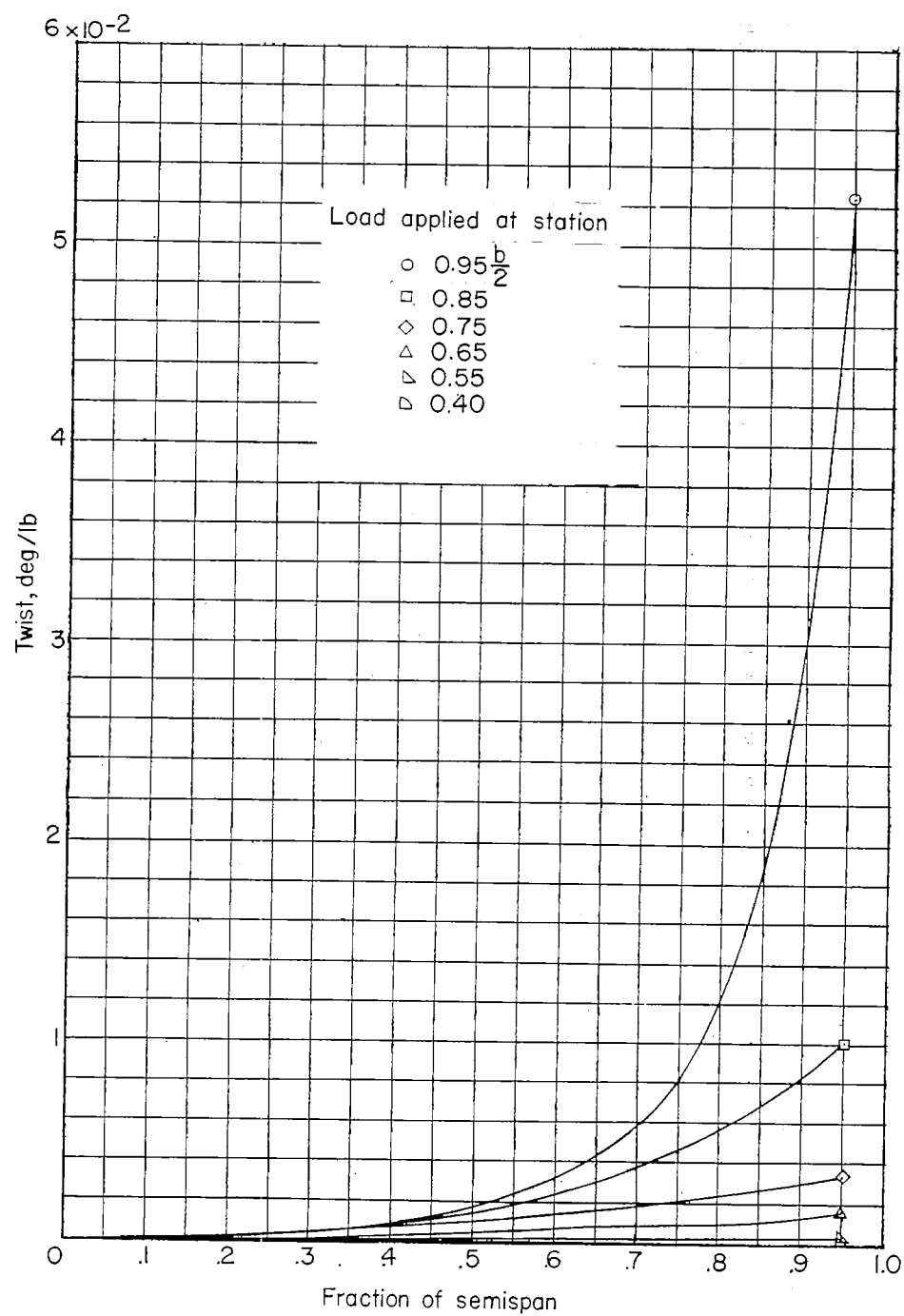
(b) Average twist from 50 to 80 percent local chord.

Figure 6.- Continued.
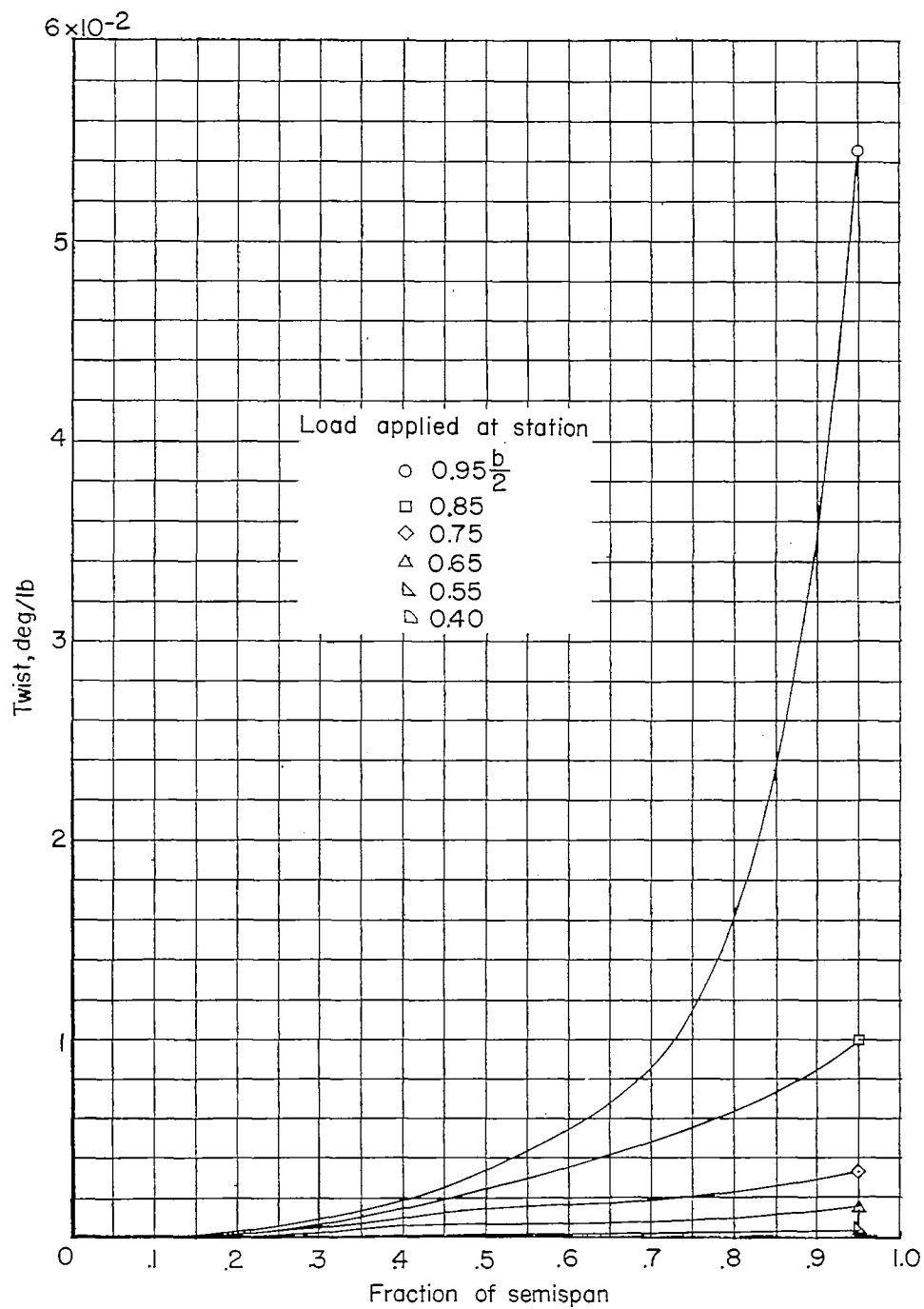
(c) Average twist from 80 to 100 percent local chord.

Figure 6.- Concluded.
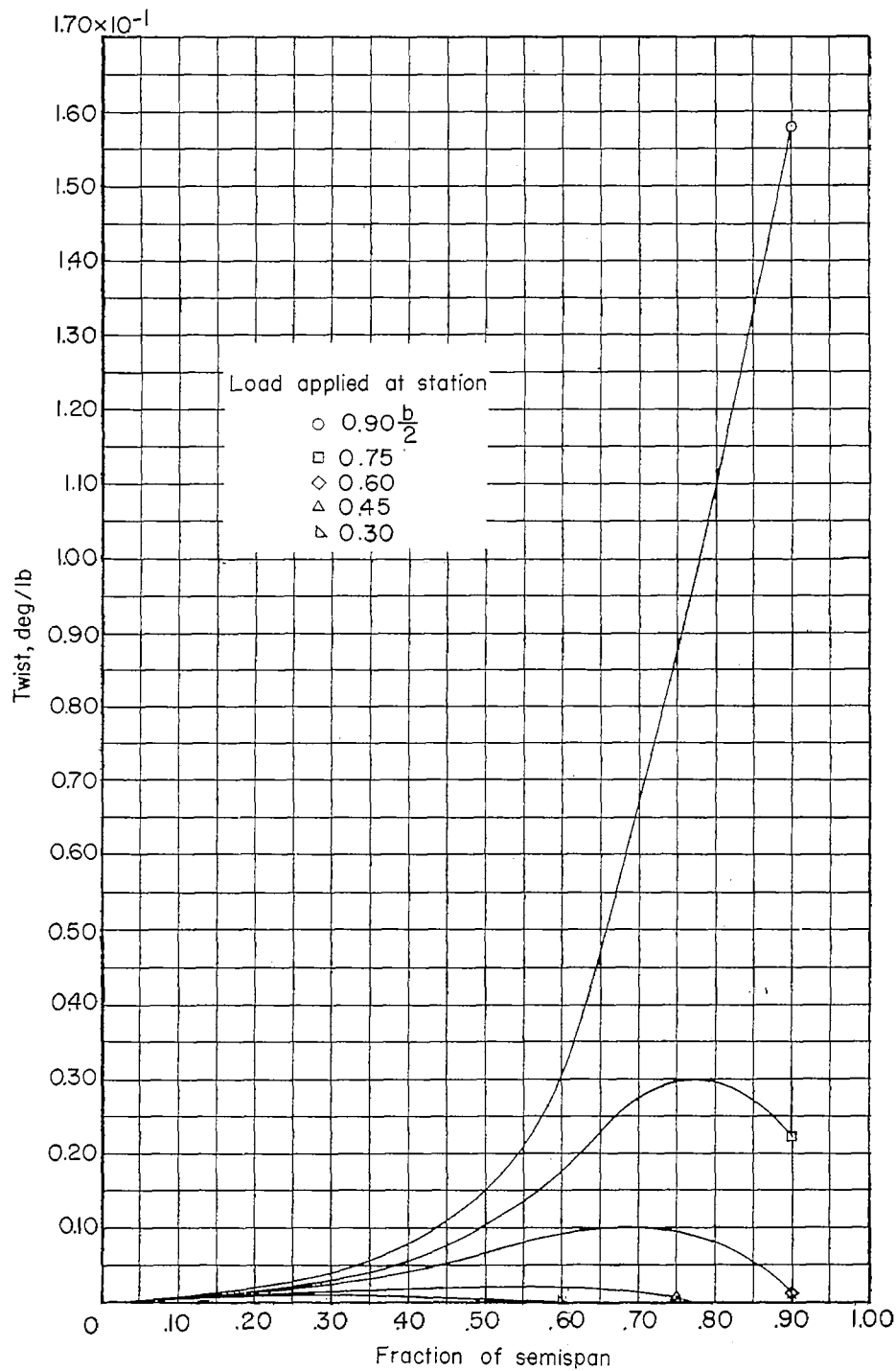
Figure 7.- Tail streamwise average twist resulting from a concentrated load applied along 50-percent-chord line.
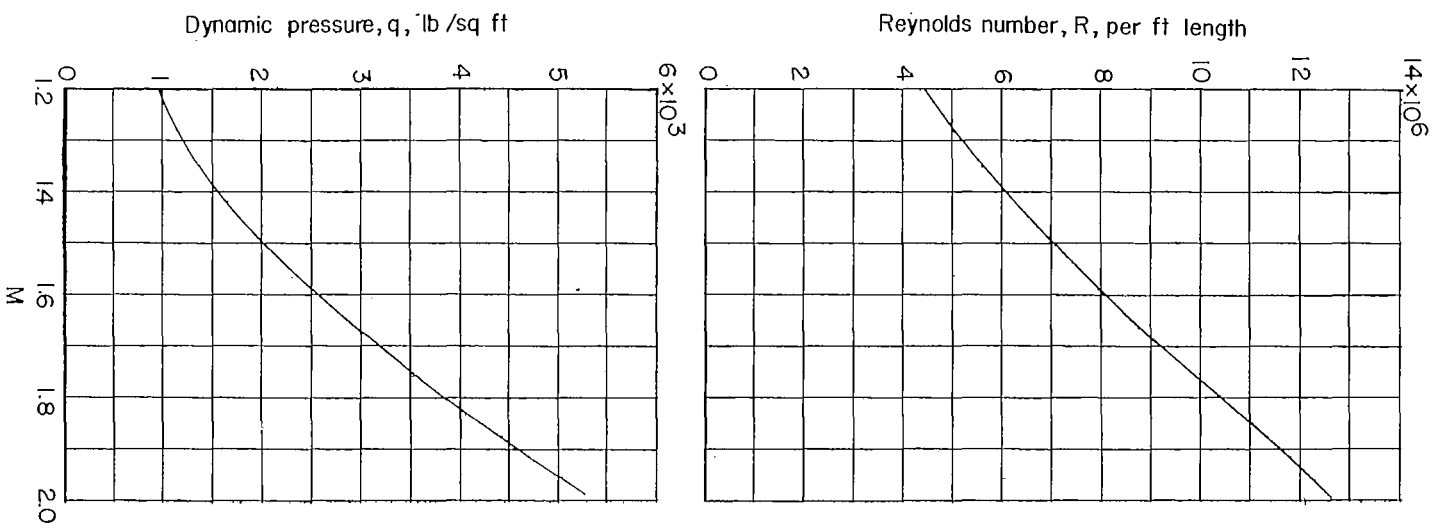
Figure 8.- Flight test conditions.
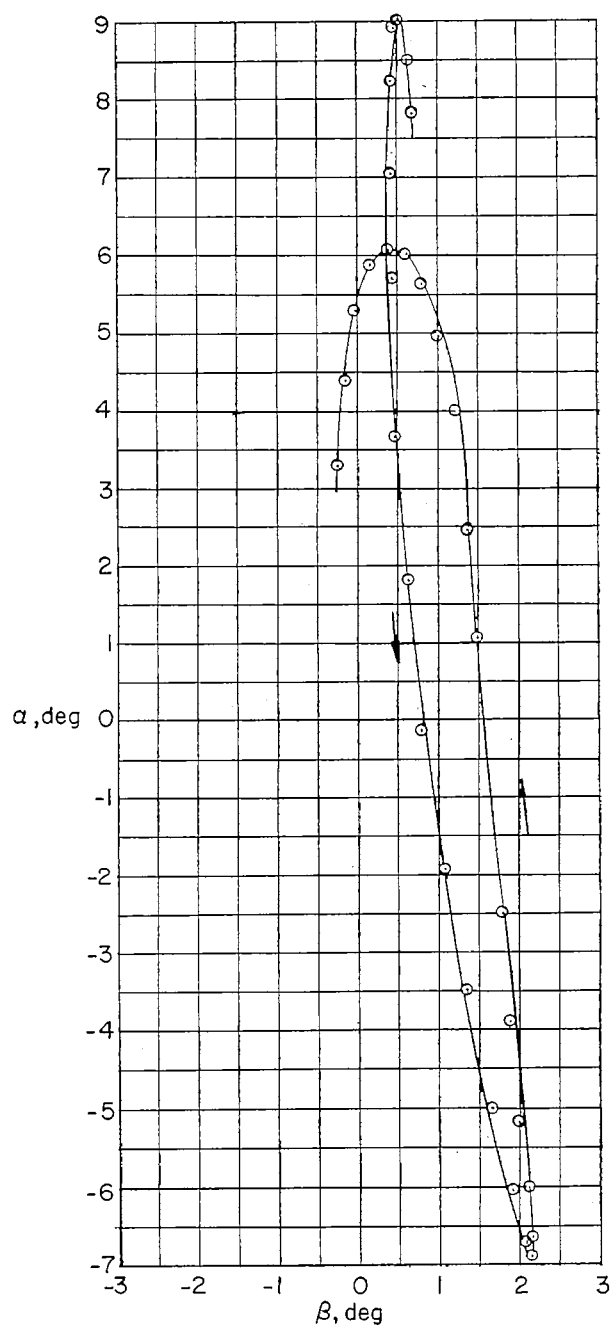
(a) Mach number, 1.24.

Figure 9.- Variation of angle of attack with sideslip angle. Model
pulsed in pitch.
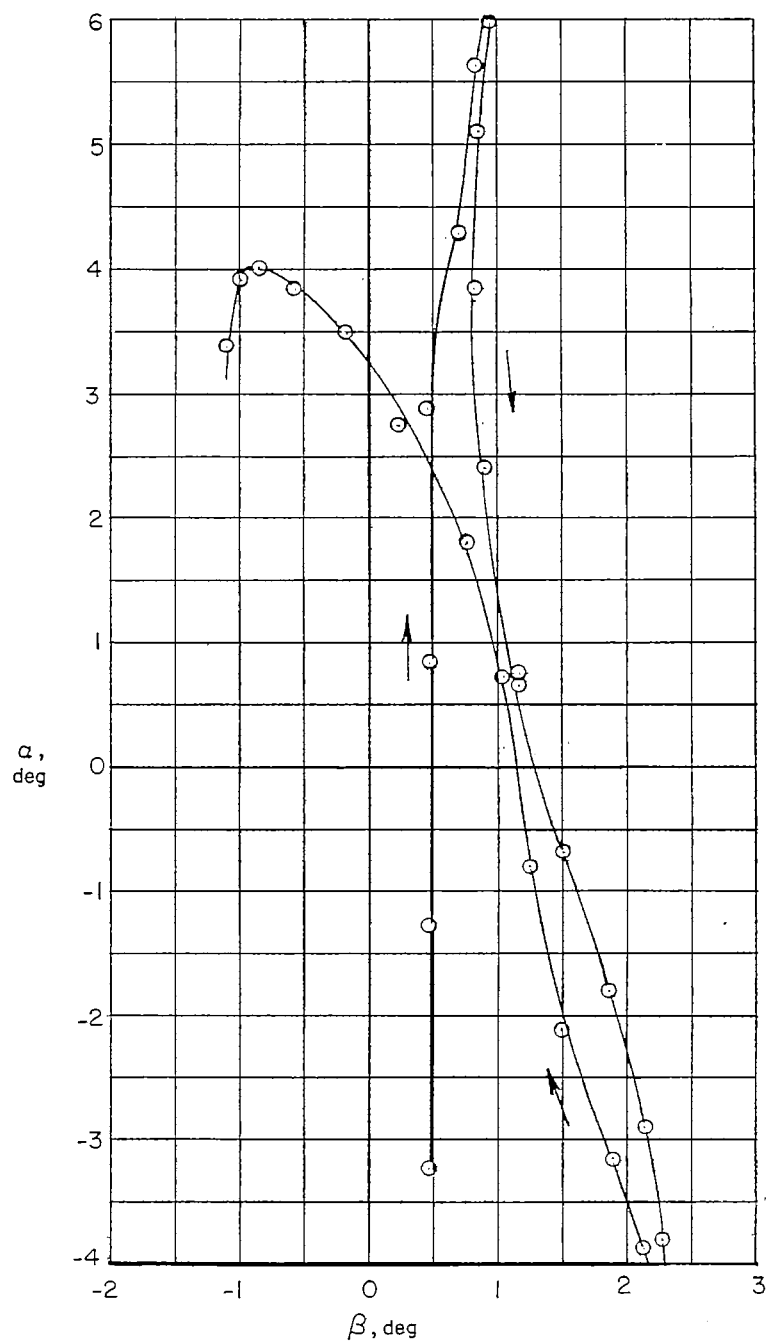
(b) Mach number, 1.46.

Figure 9.- Continued.
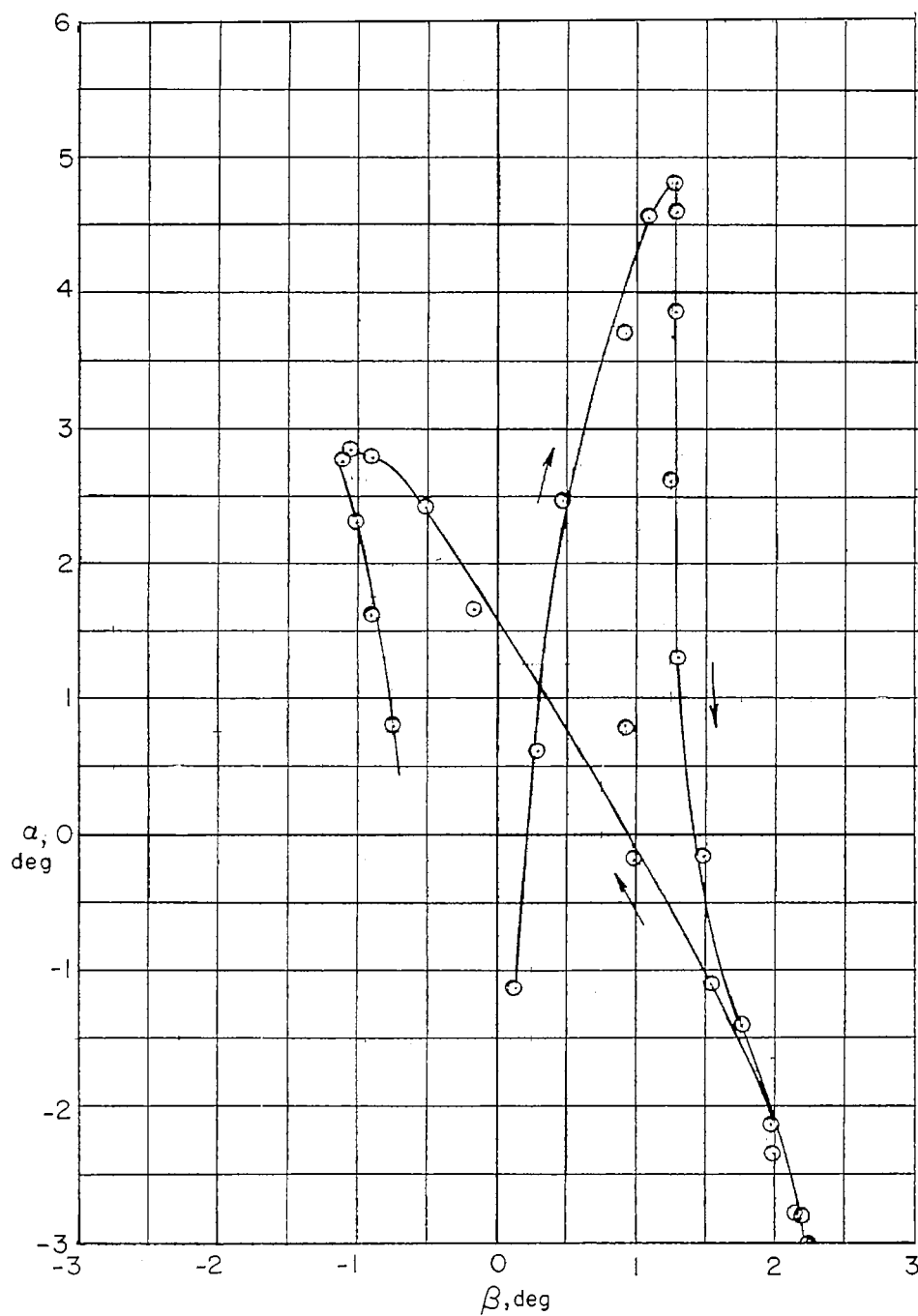
(c) Mach number, 1.69.

Figure 9.- Continued.
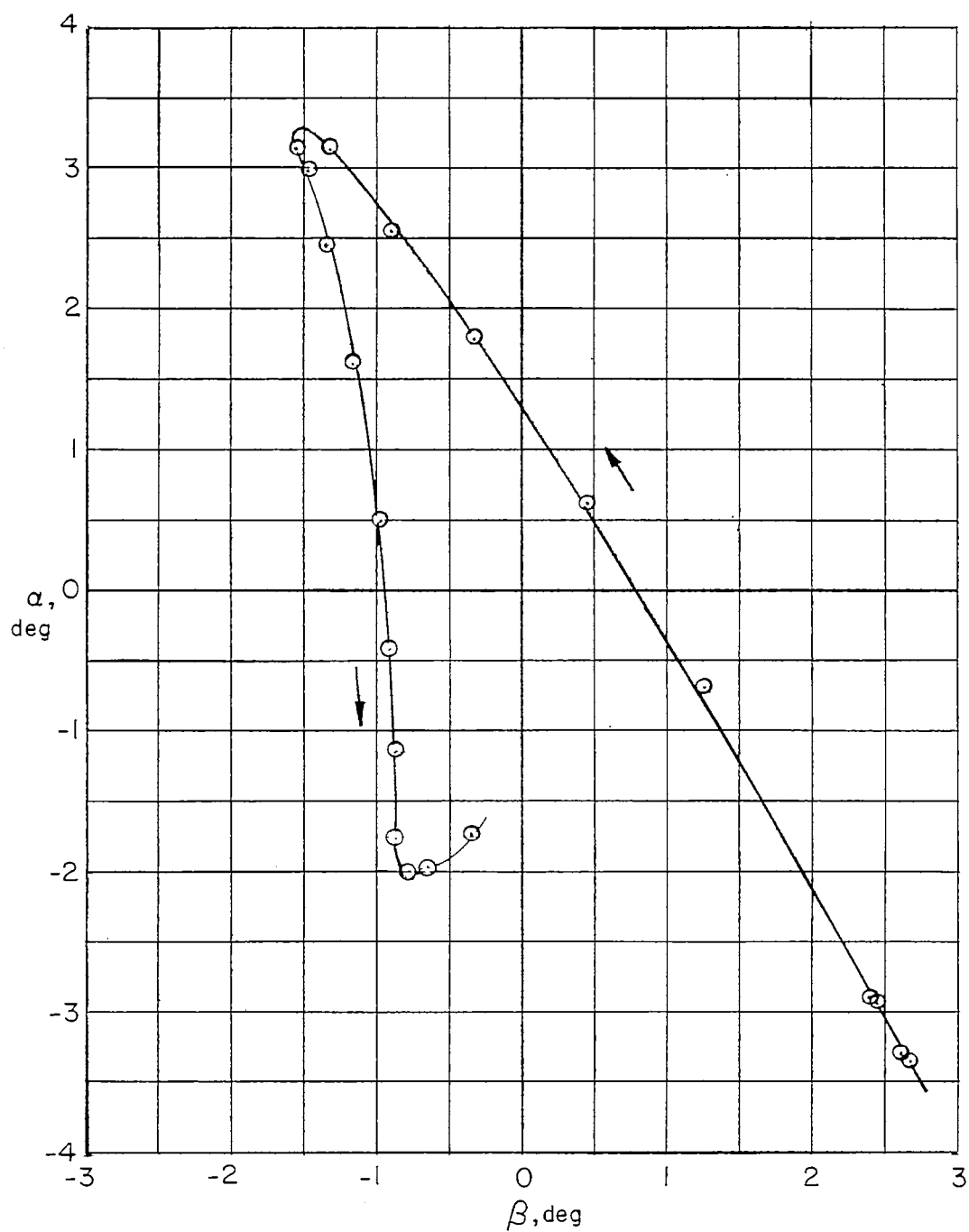
(d) Mach number, 1.81.

Figure 9.- Concluded.
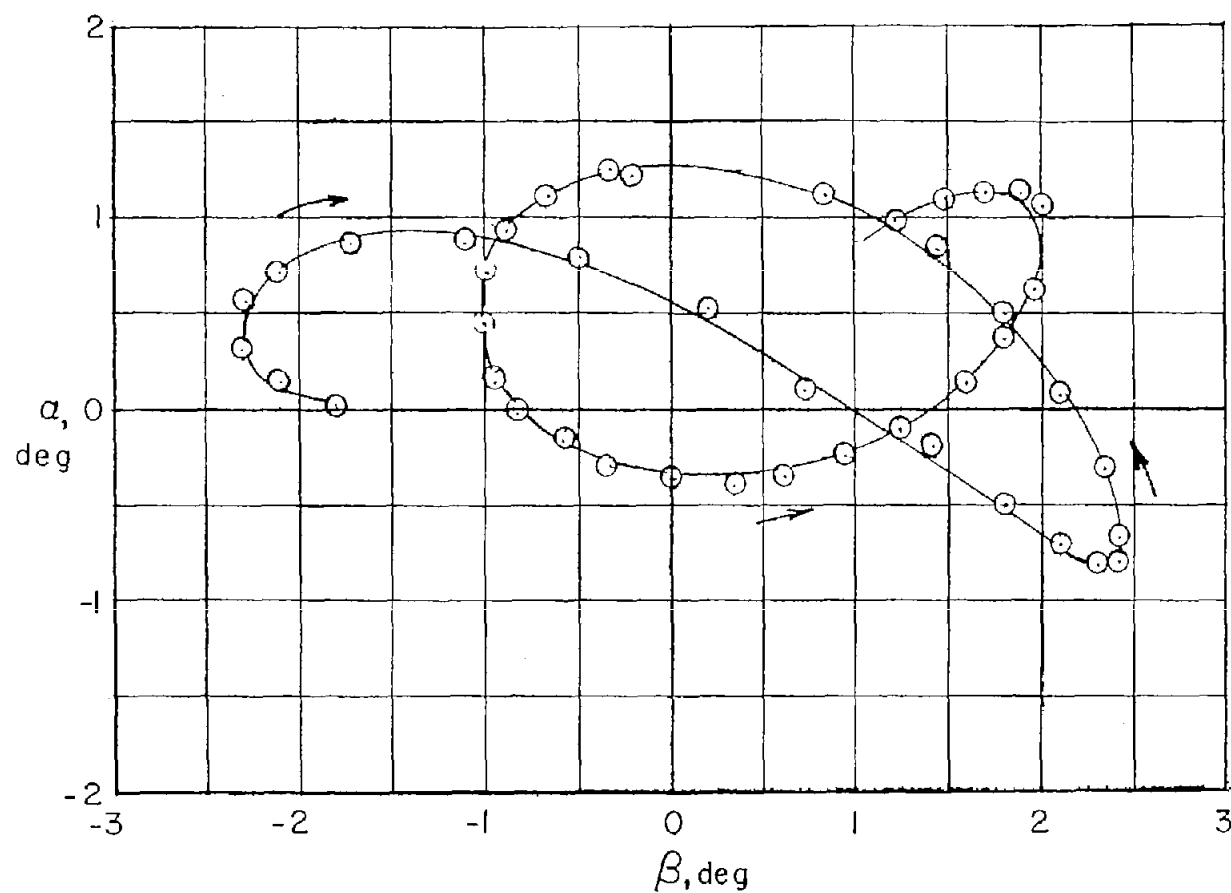
(a) Mach number, 1.59.

Figure 10.- Variation of angle of attack with sideslip angle. Model pulsed in yaw.
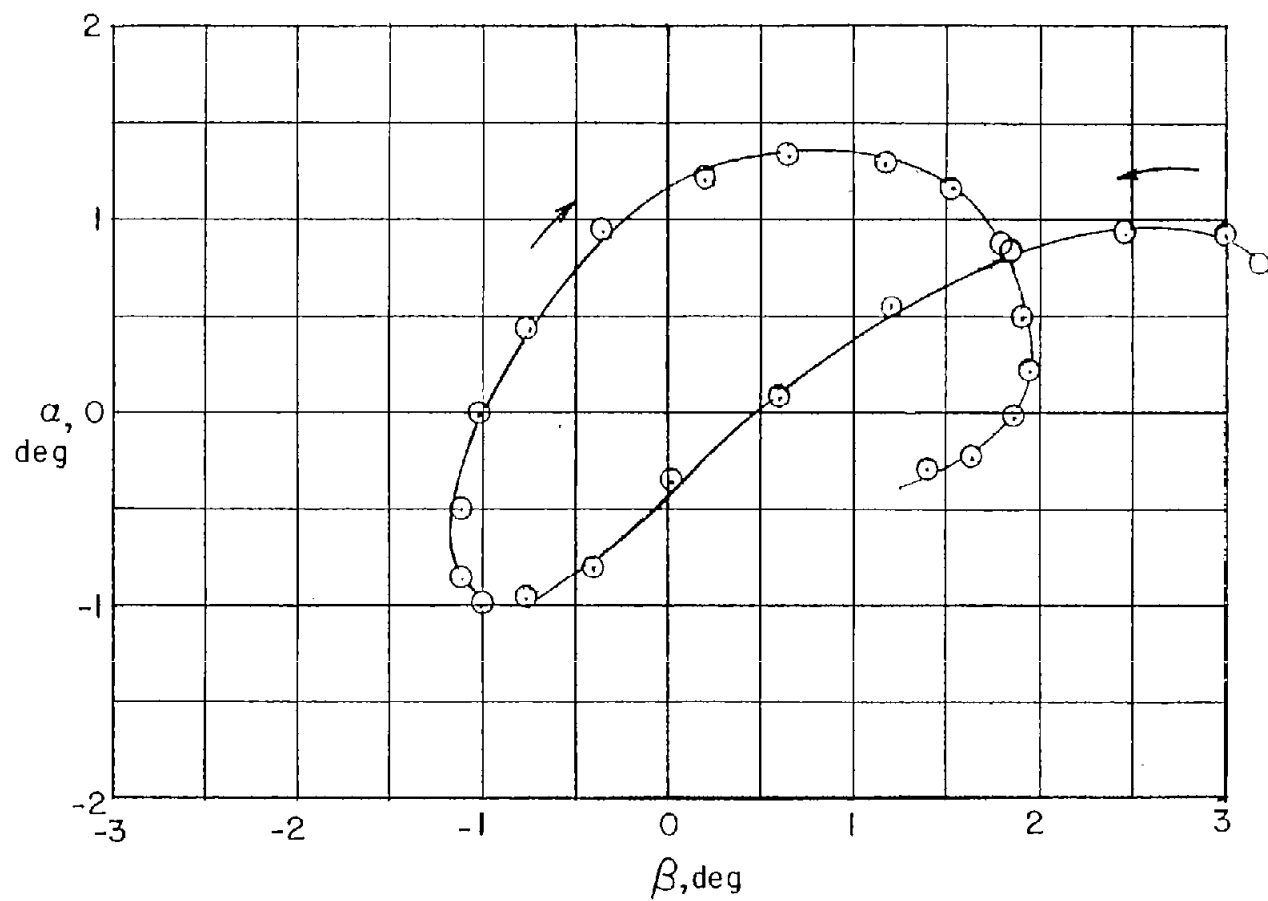
(b) Mach number, 1.86.

Figure 10.- Concluded.
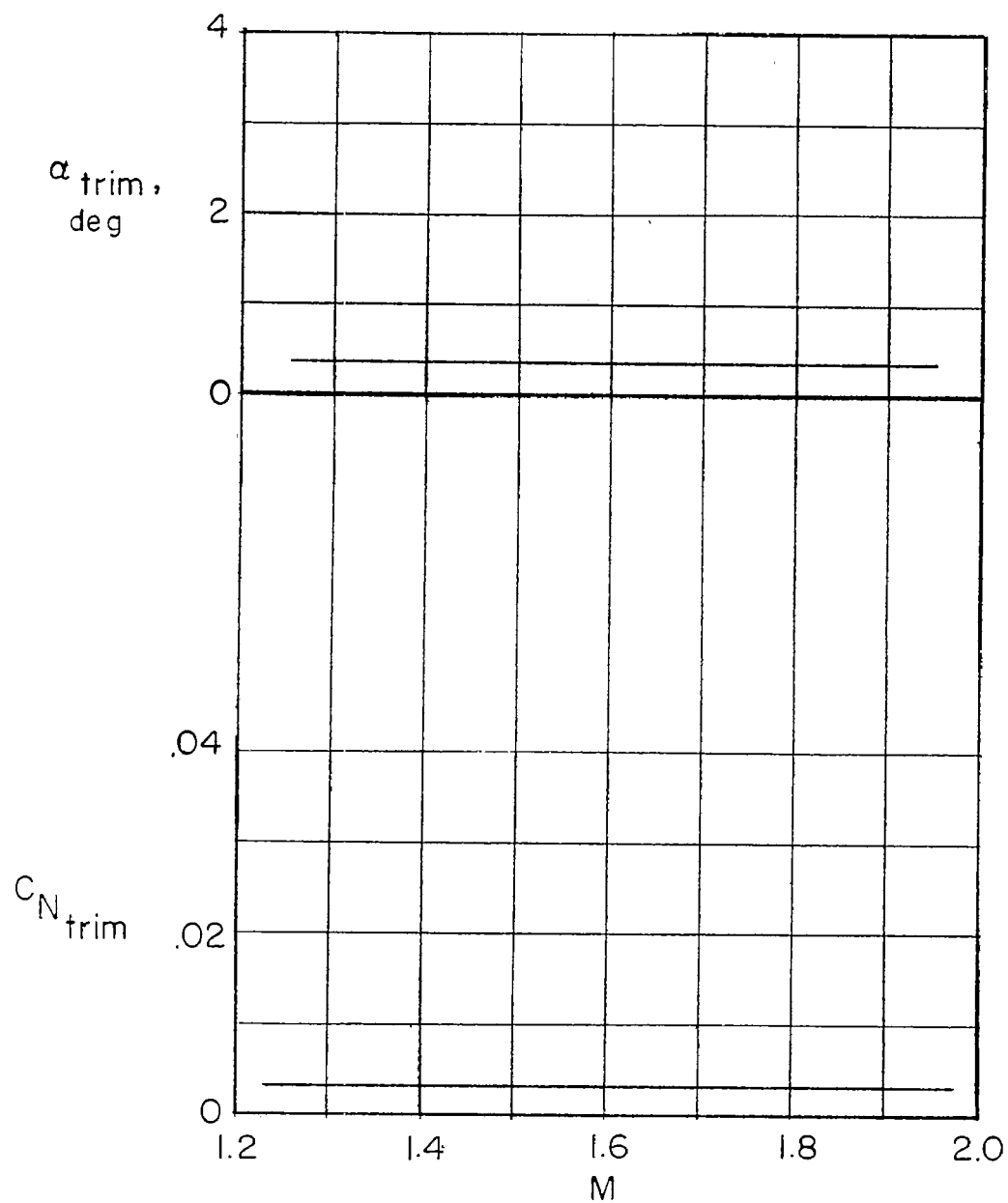
(a) Longitudinal.

Figure 11.- Model trim.
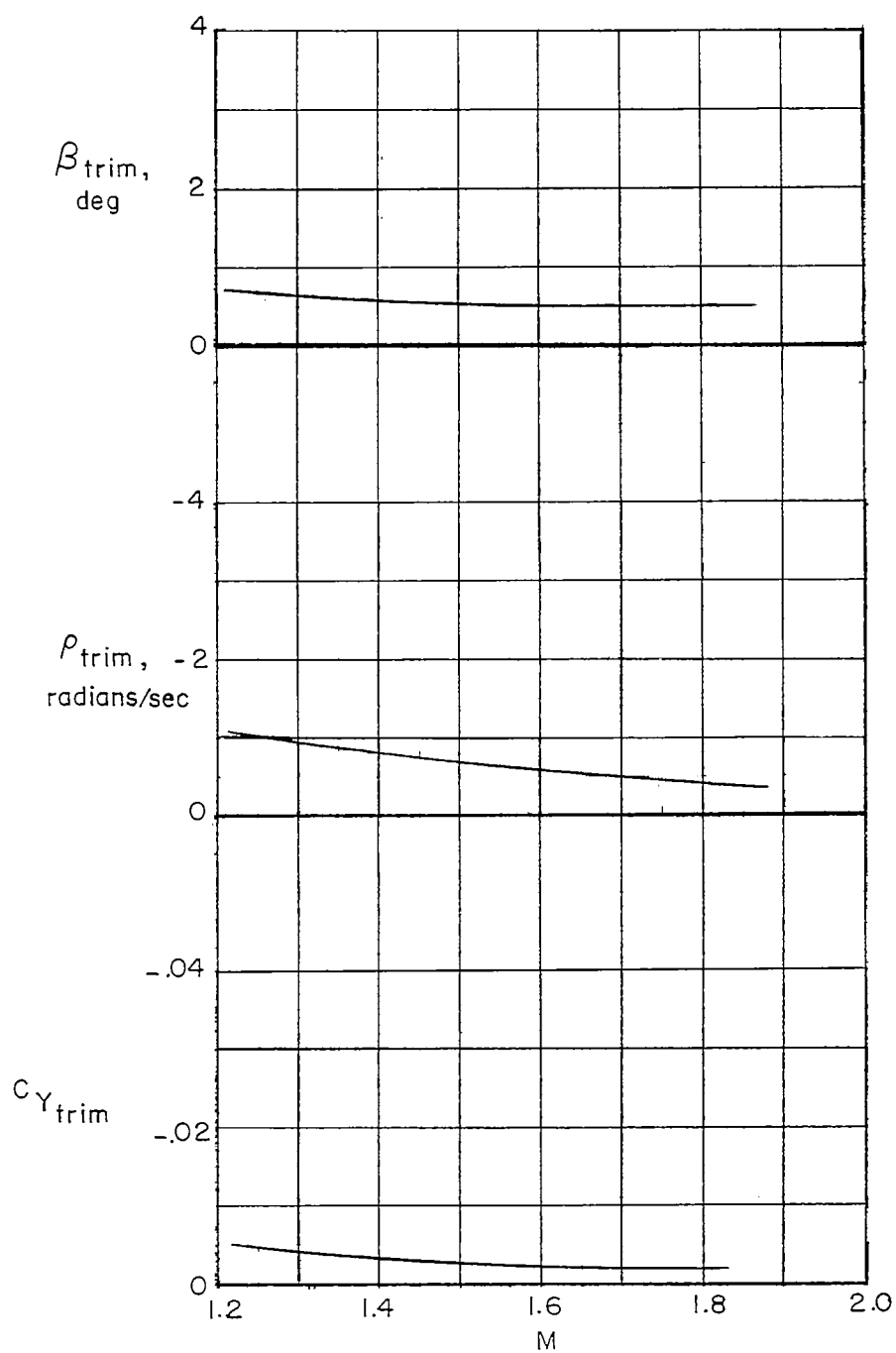
(b) Lateral.

Figure 11.- Concluded.
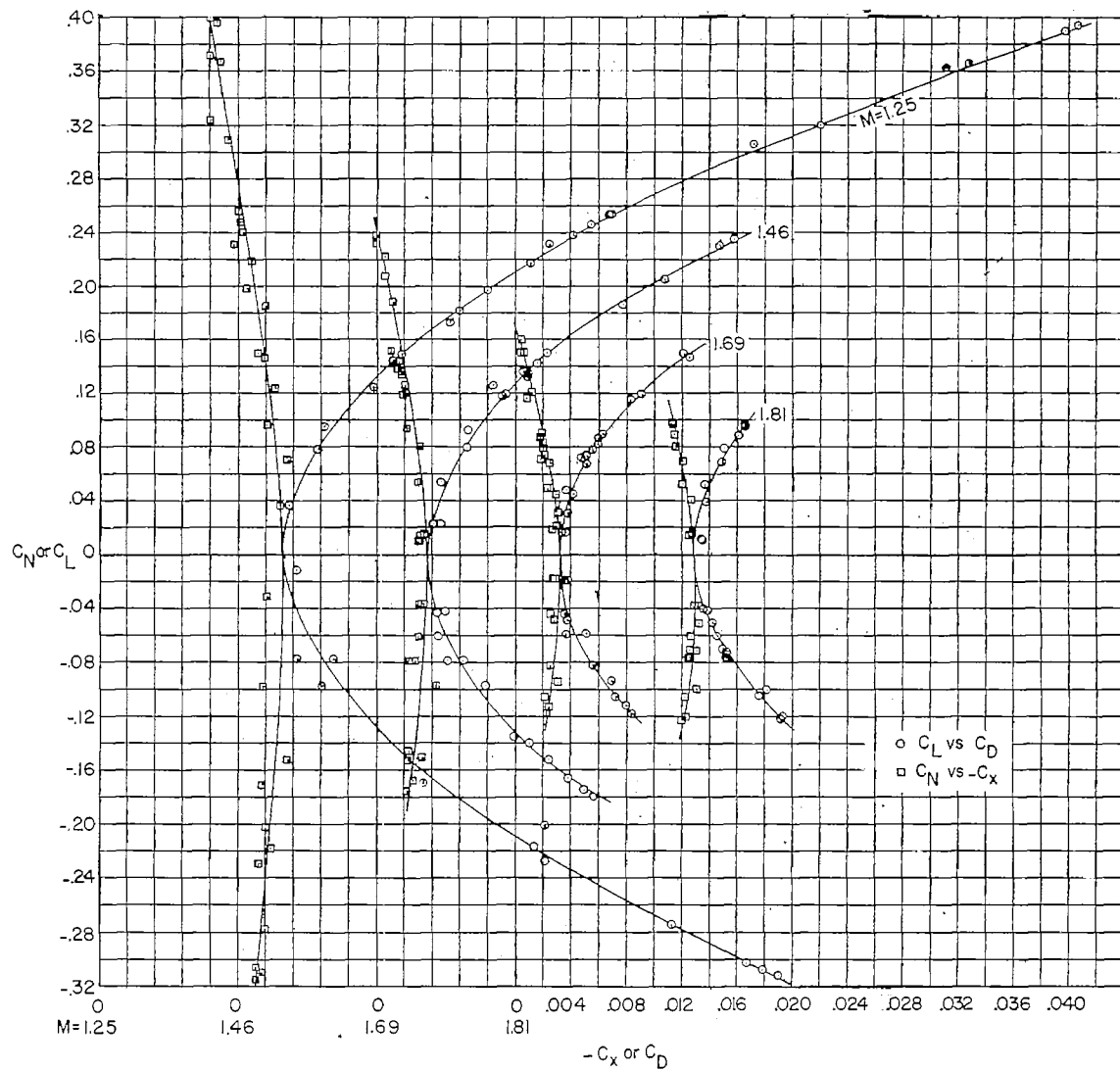
Figure 12.- Variation of normal-force coefficient with axial-force coefficient and lift coefficient with drag coefficient at constant Mach numbers.
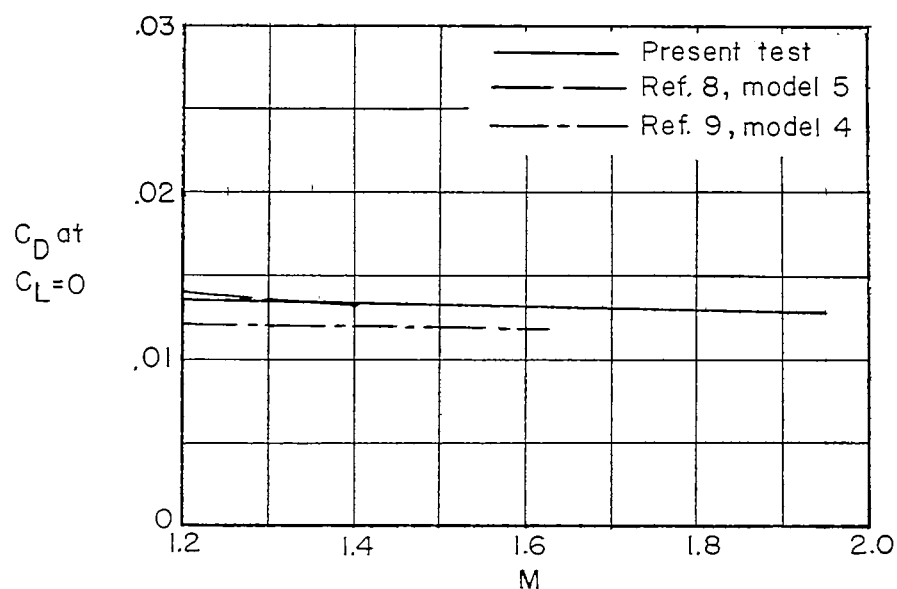
(a) Drag coefficient at $C_L = 0$.
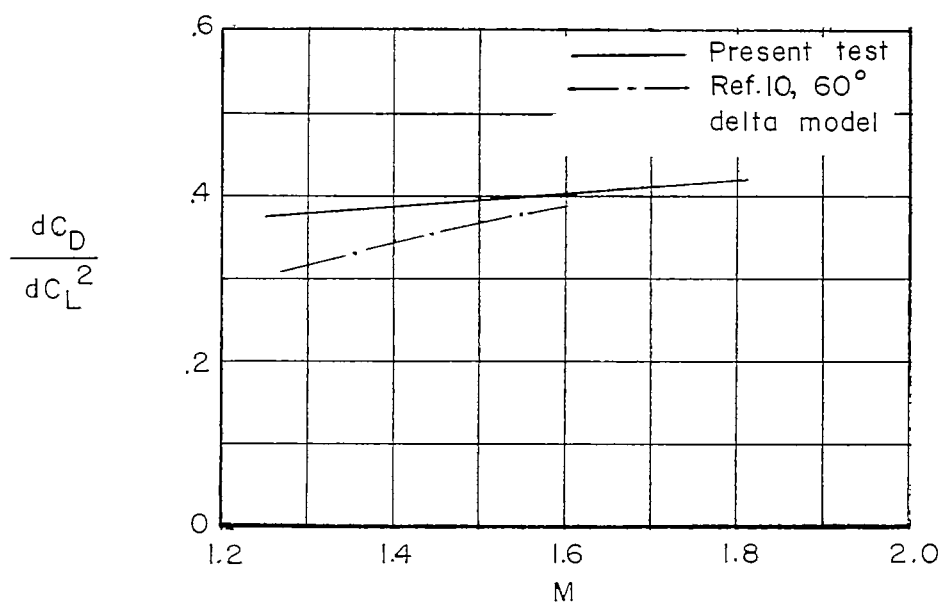
(b) Drag-due-to-lift parameter dC_D/dC_L^2.

Figure 13.- Drag coefficient at zero lift and drag-due-to-lift parameter plotted against Mach number.
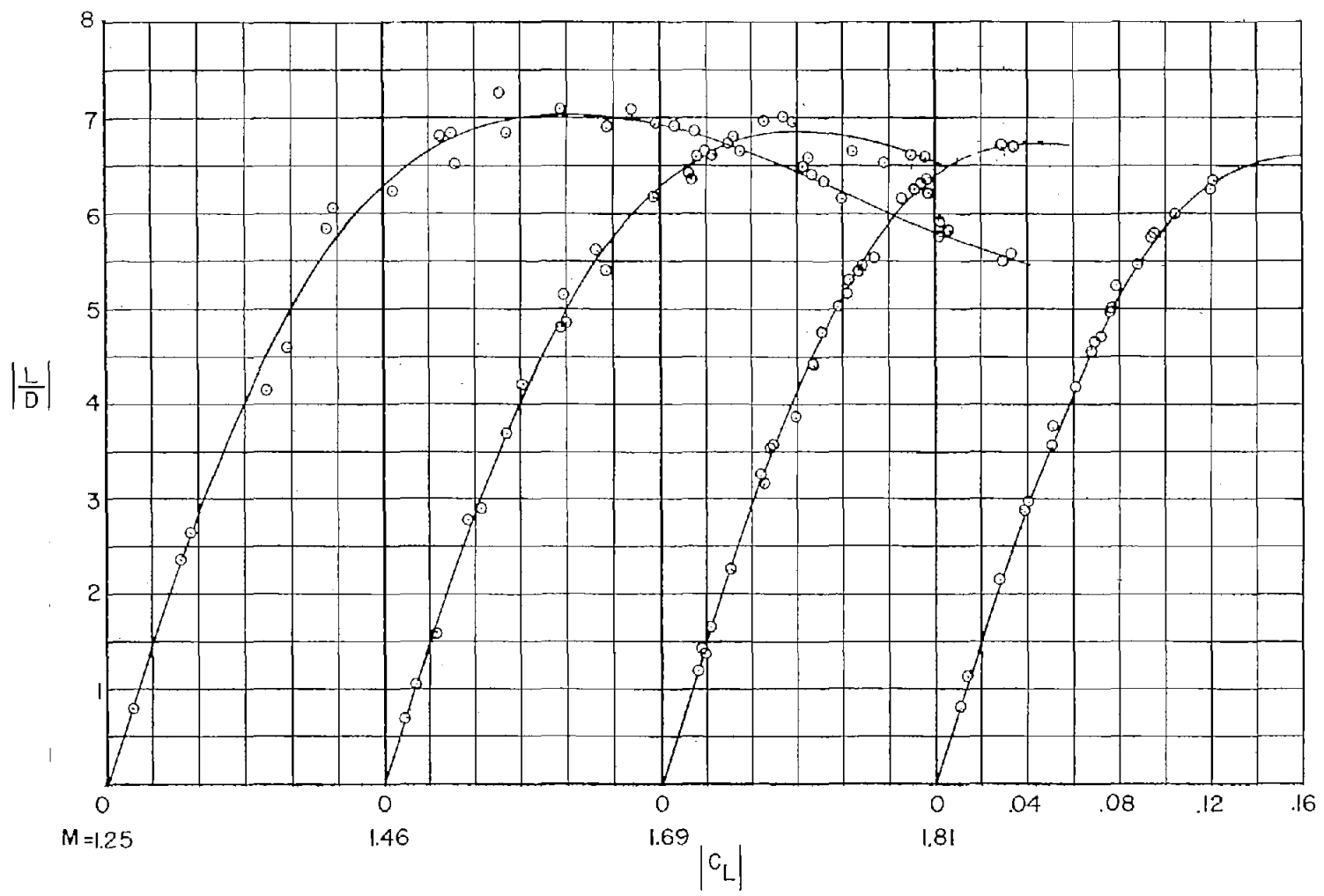
Figure 14.- Lift-drag ratio plotted against lift coefficient.
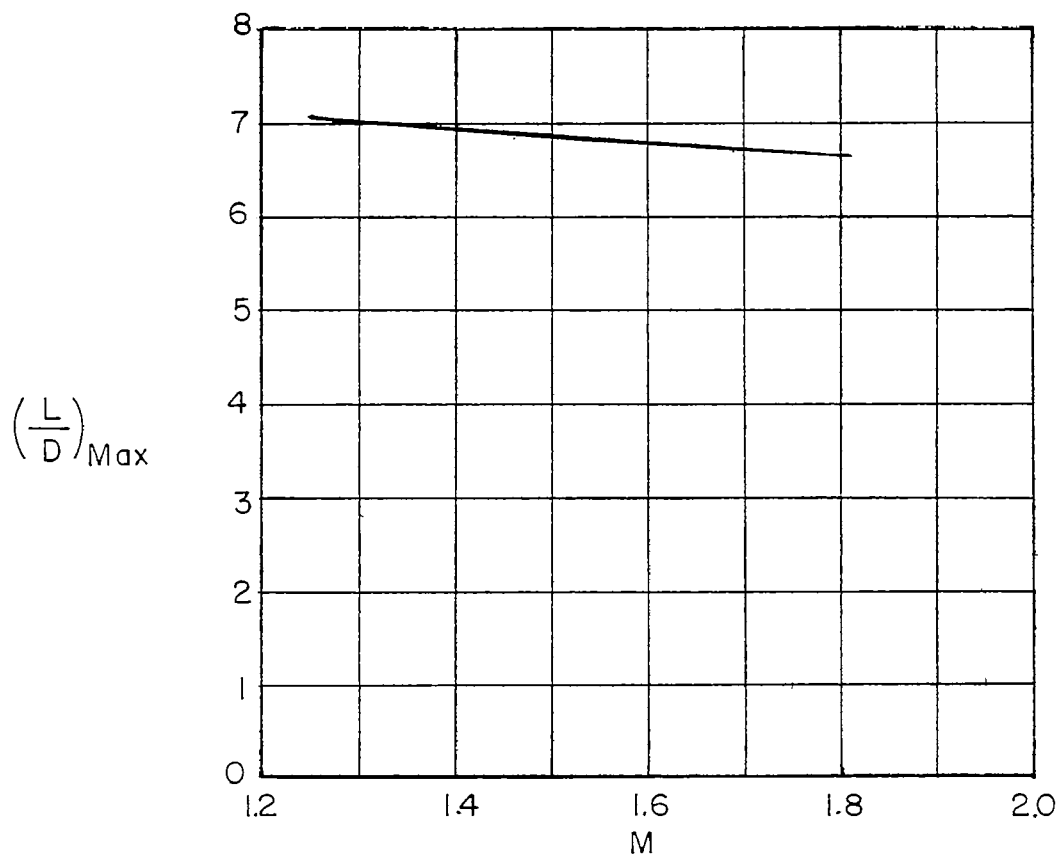
(a) Maximum lift-drag ratio.
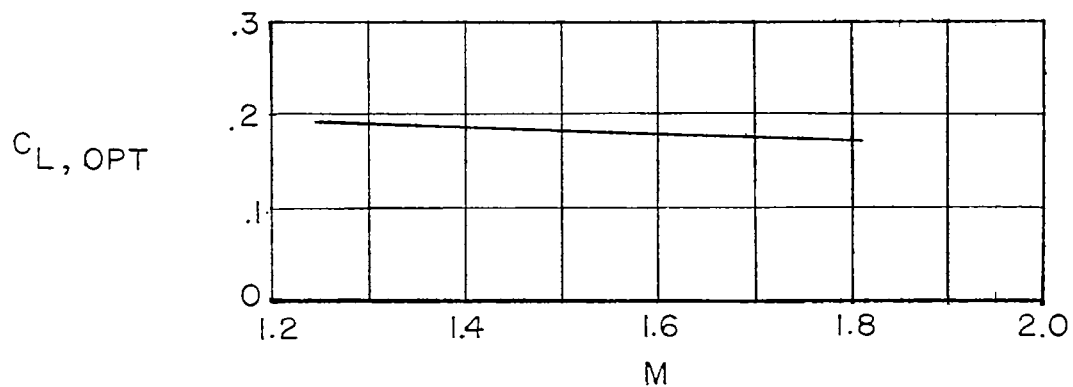
(b) Lift coefficient at $(L/D)_{max}$.

Figure 15.- Maximum lift-drag ratio and optimum lift coefficient plotted against Mach number.
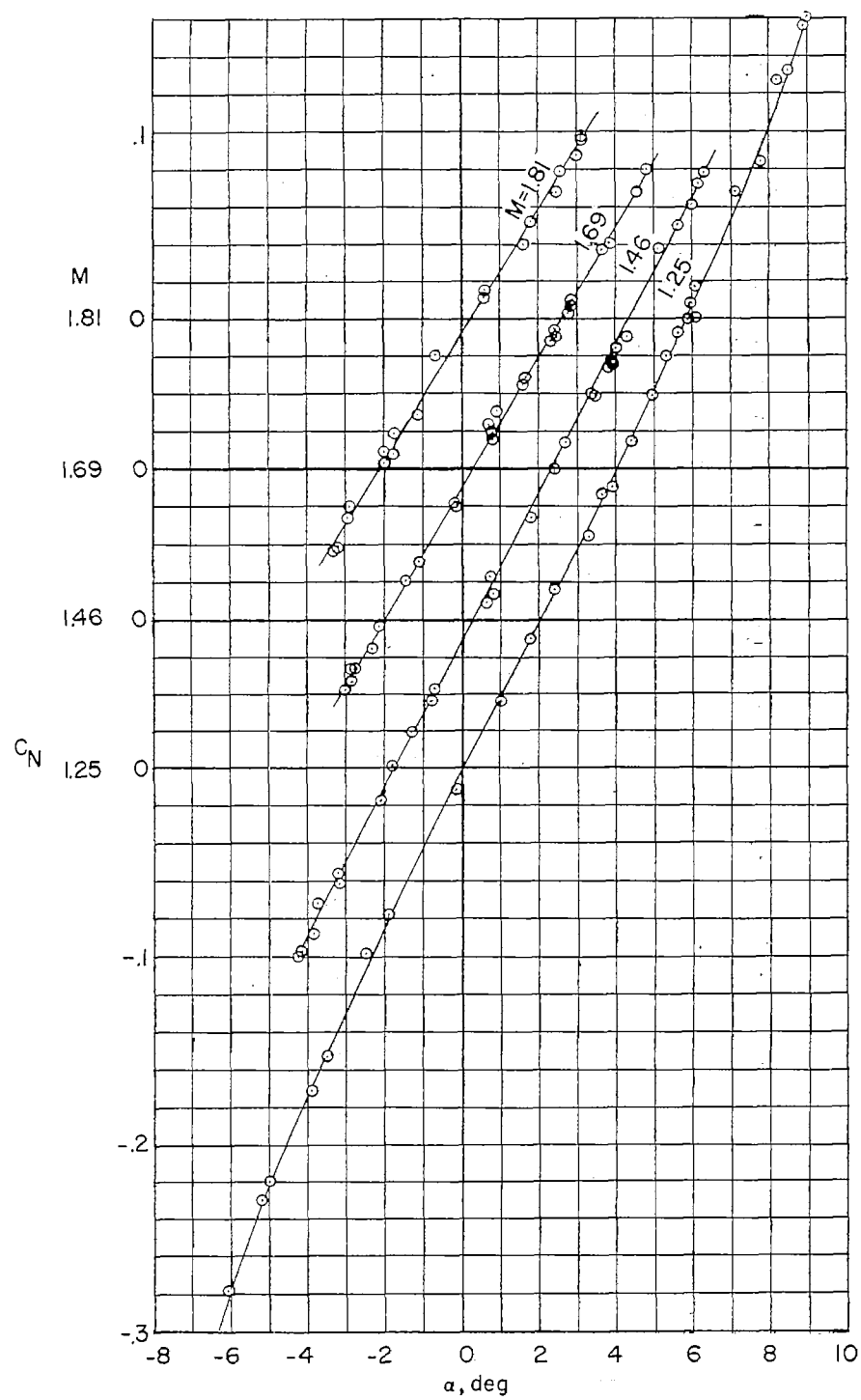
Figure 16.- Variation of normal-force coefficient with angle of attack.
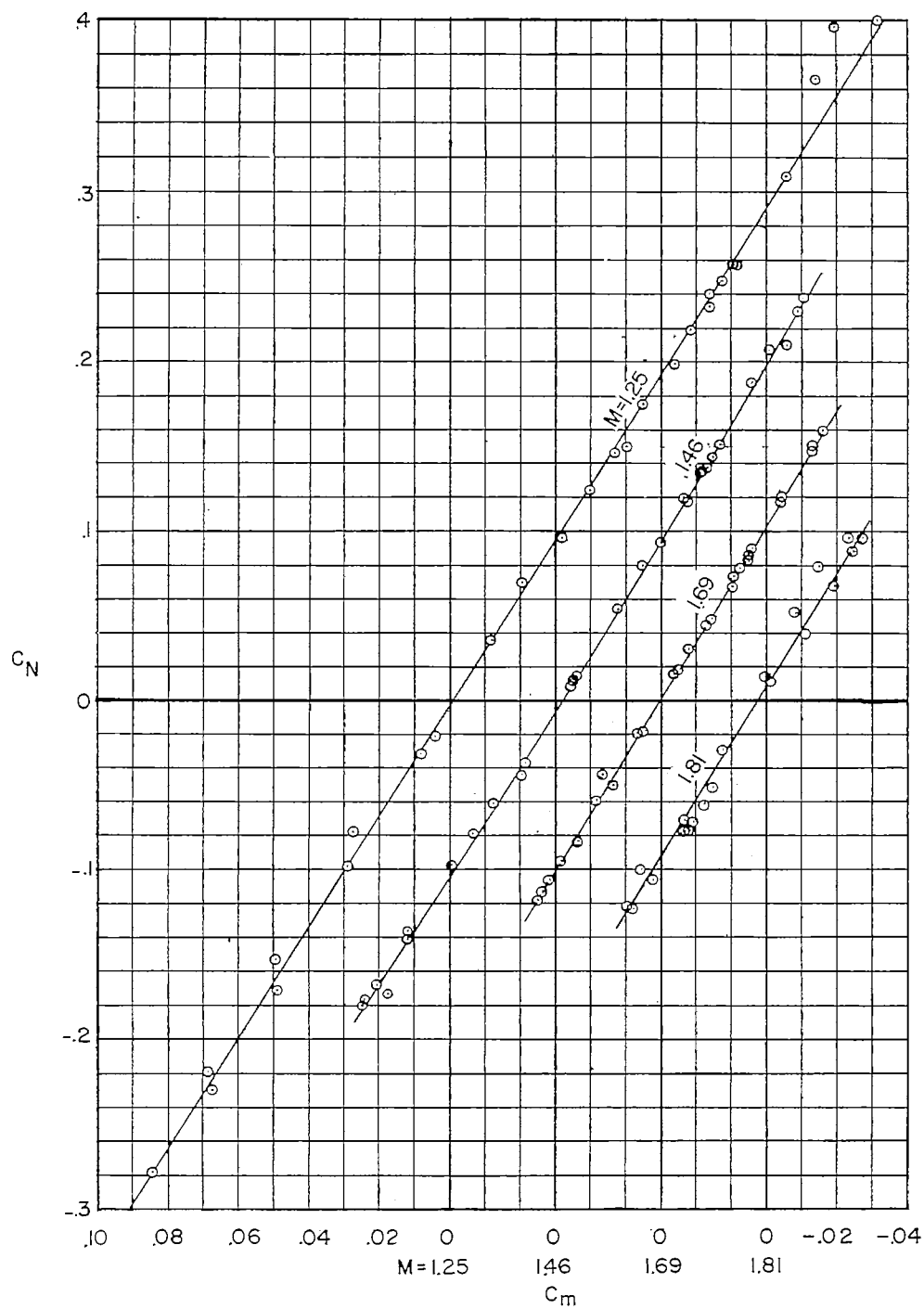
Figure 17.- Variation of normal-force coefficient with pitching-moment coefficient.
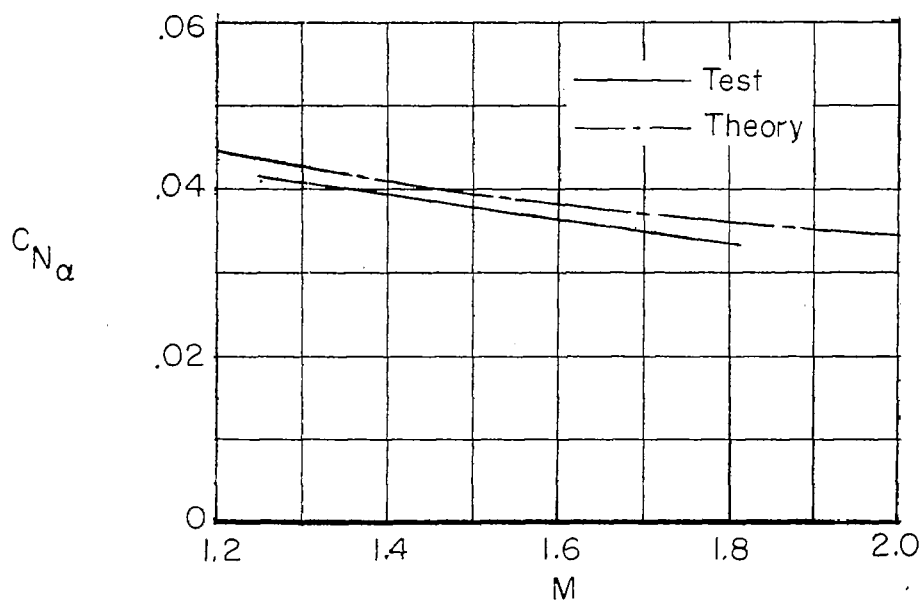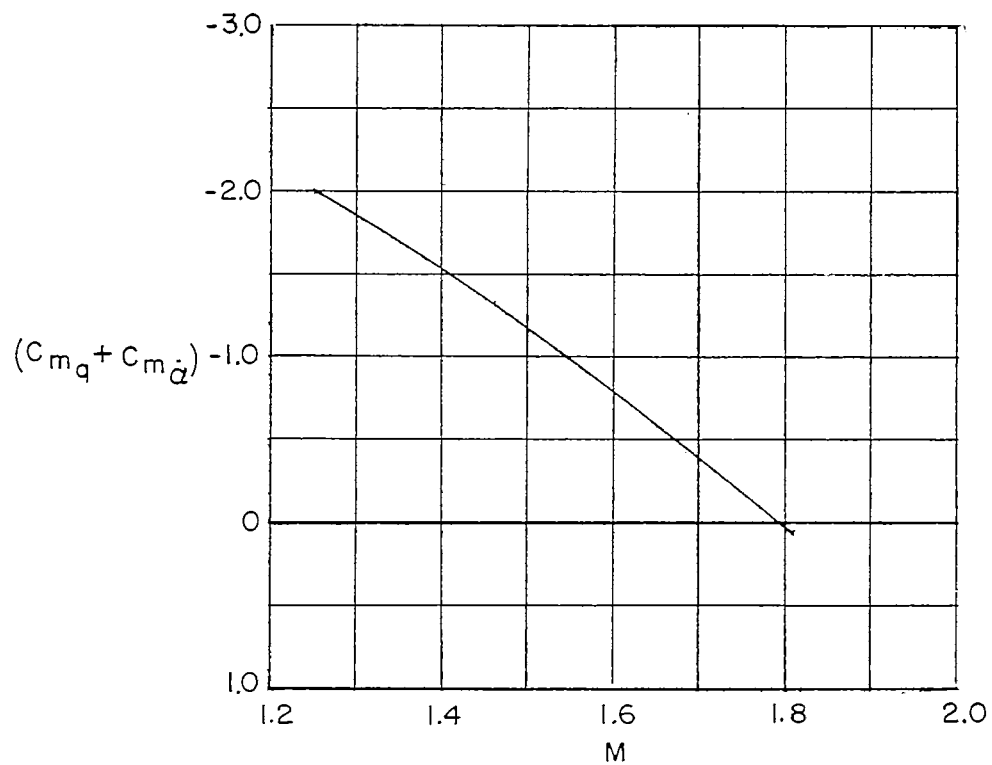
(a) Normal-force-curve slope C_{N_α}.
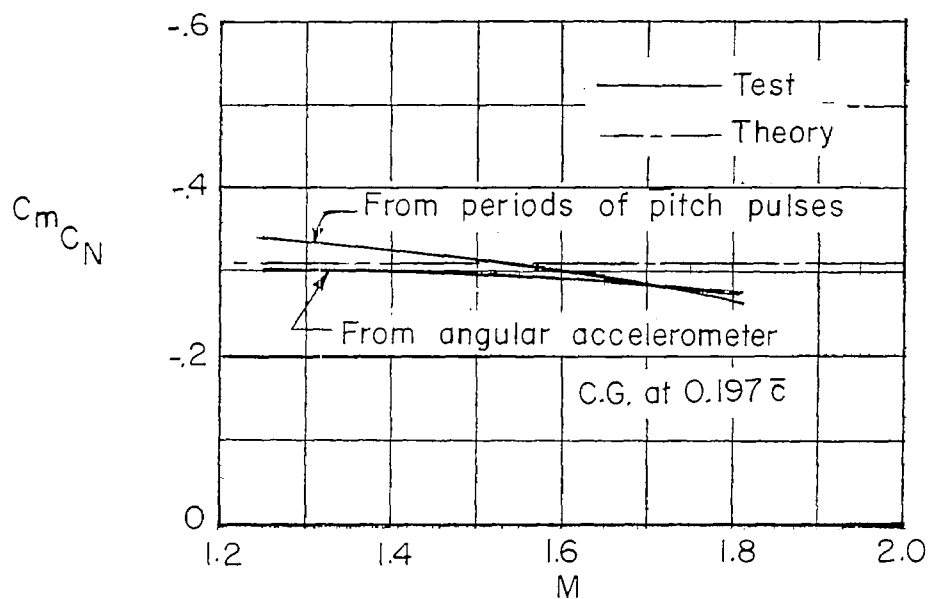
(b) Static stability parameter in pitch $C_{m_{C_N}}$.

Figure 18.- Variation of lift effectiveness and static stability parameters with Mach number.
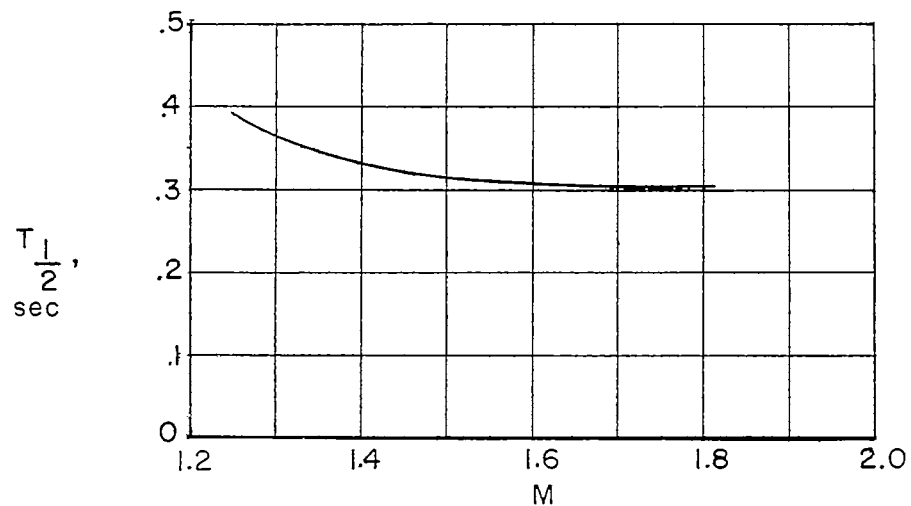
(a) Time for pitching oscillation to damp to one-half amplitude.
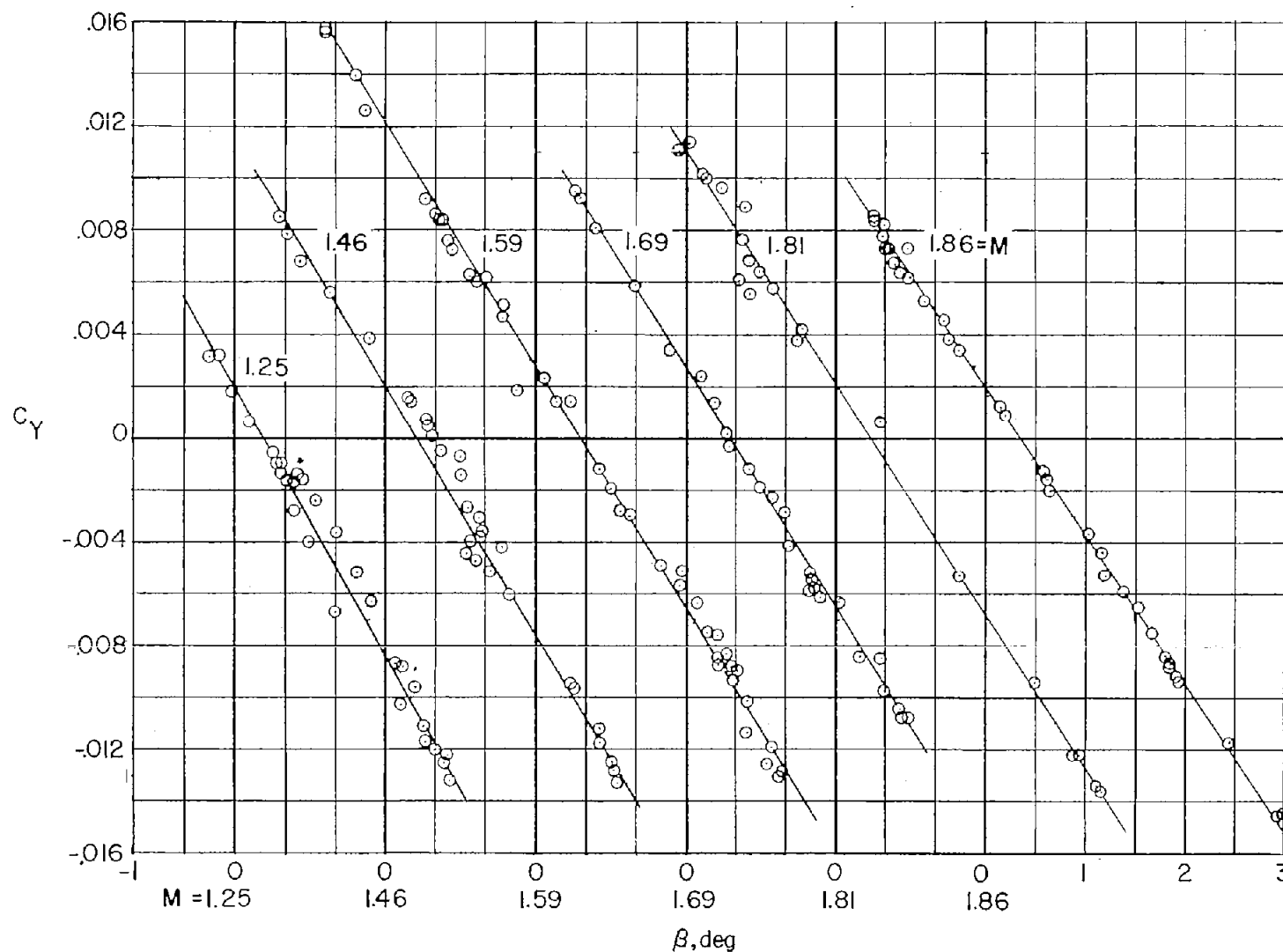

(b) Rotary damping derivatives.

Figure 19.- Damping in pitch.

Figure 20.- Variation of side-force coefficient with angle of sideslip.

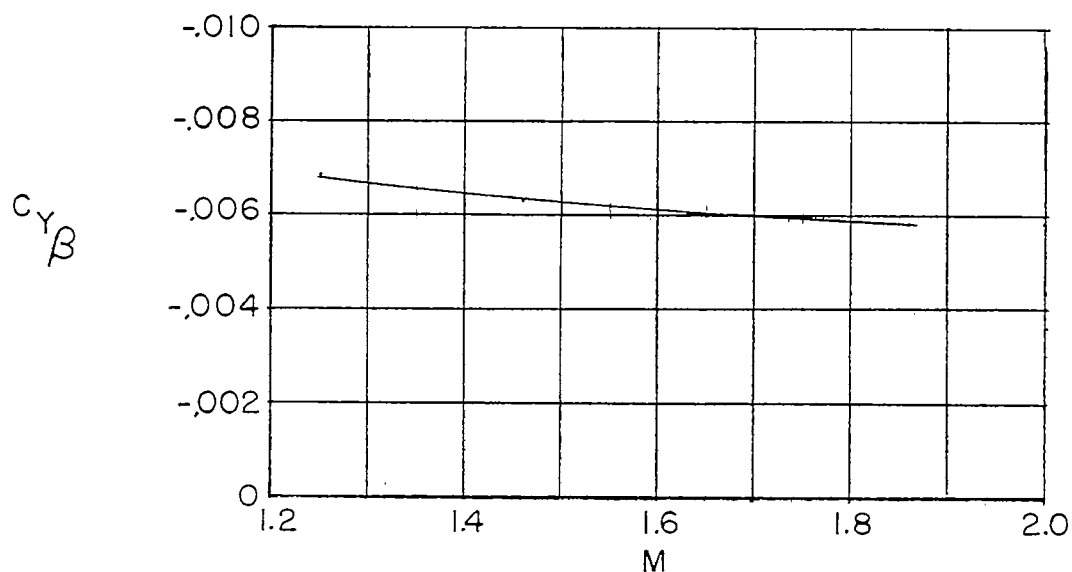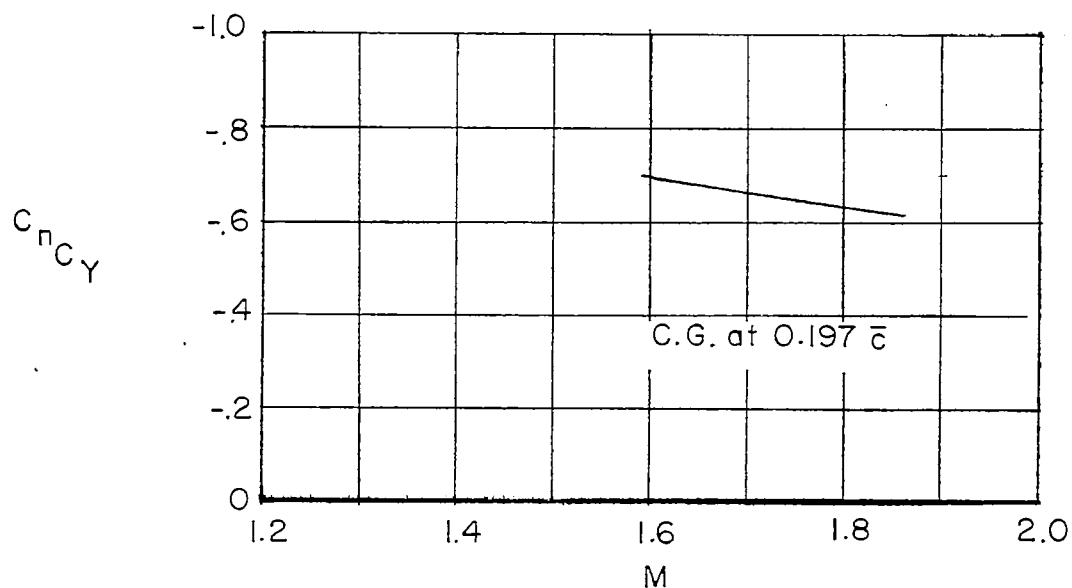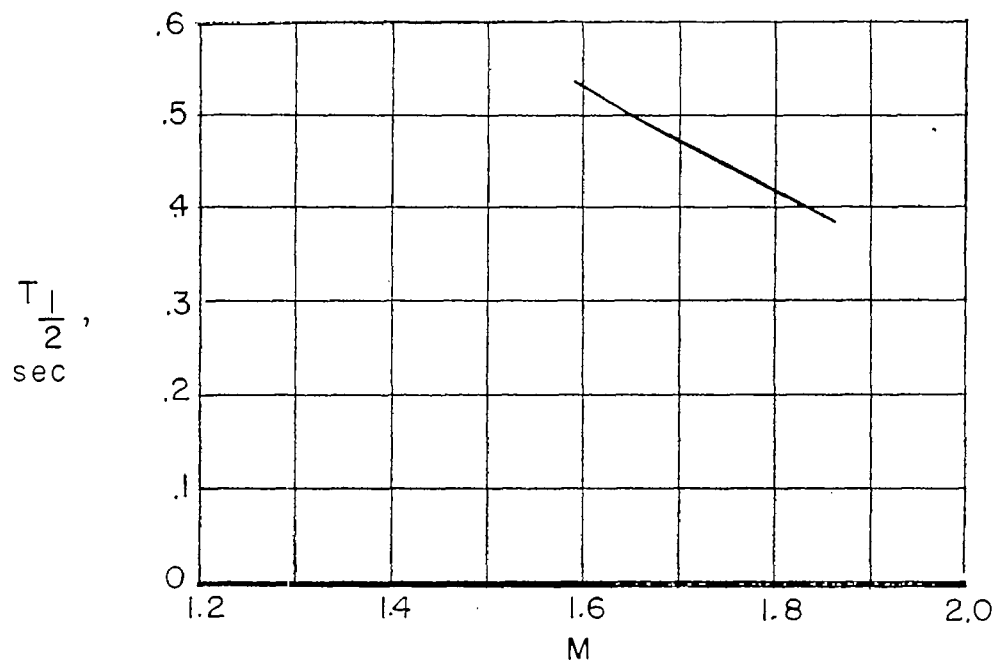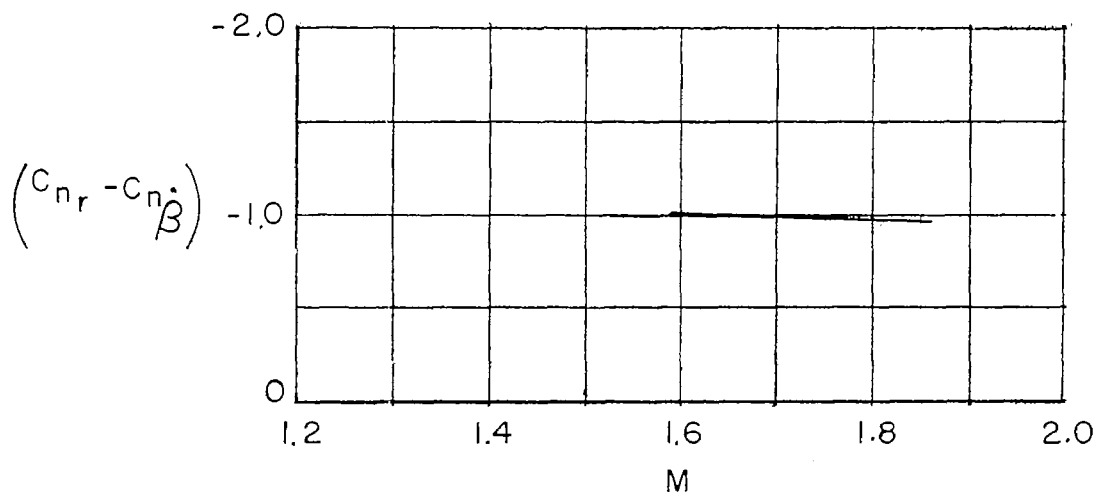(a) Side-force-curve slope C_{Y_β}.

C.G. at $0.197\ \bar{c}$

(b) Static stability parameter in yaw $C_{n_{C_Y}}$.

Figure 21.- Variation of side-force effectiveness and static directional stability parameters with Mach number.

(a) Time for yawing oscillation to damp to one-half amplitude.

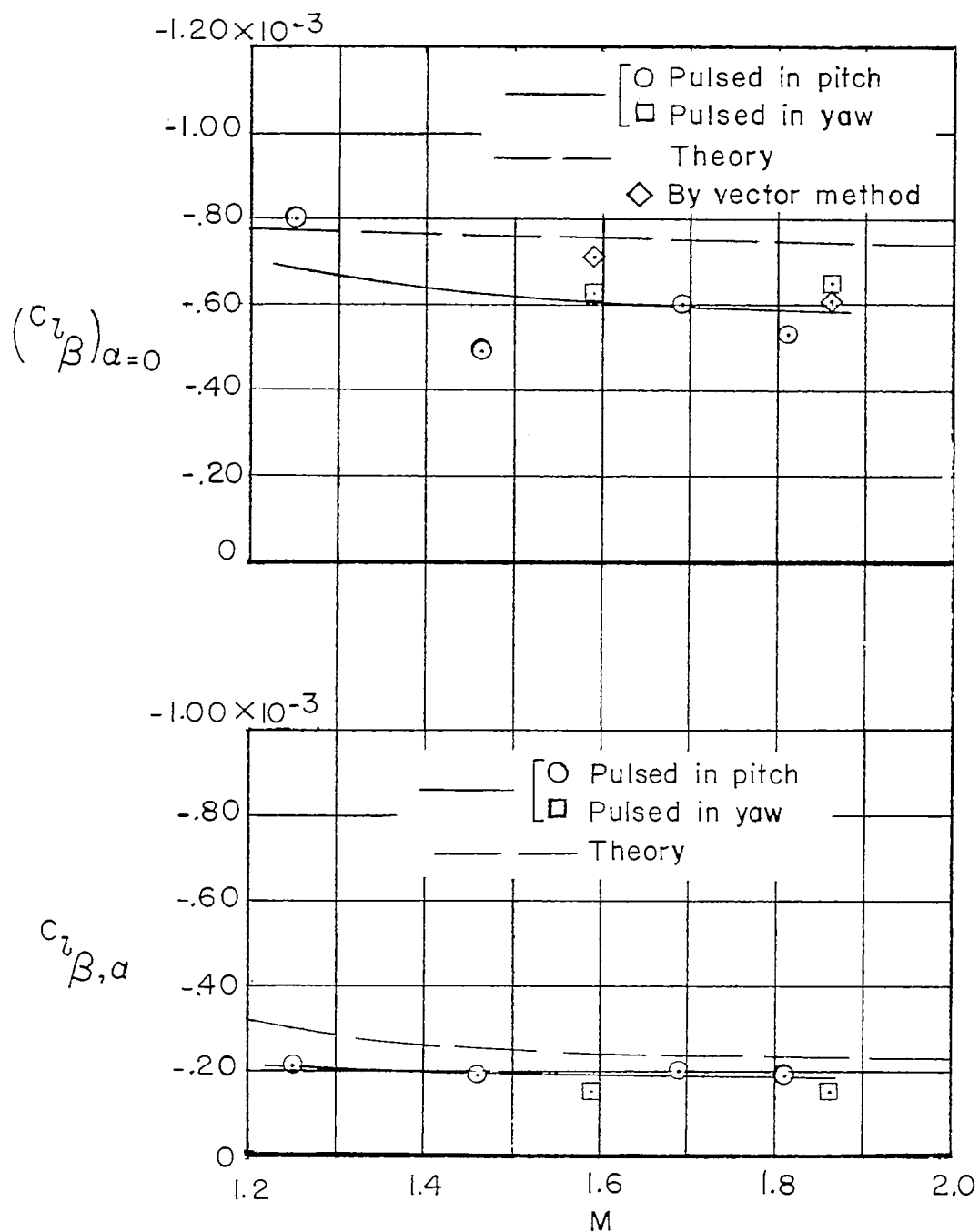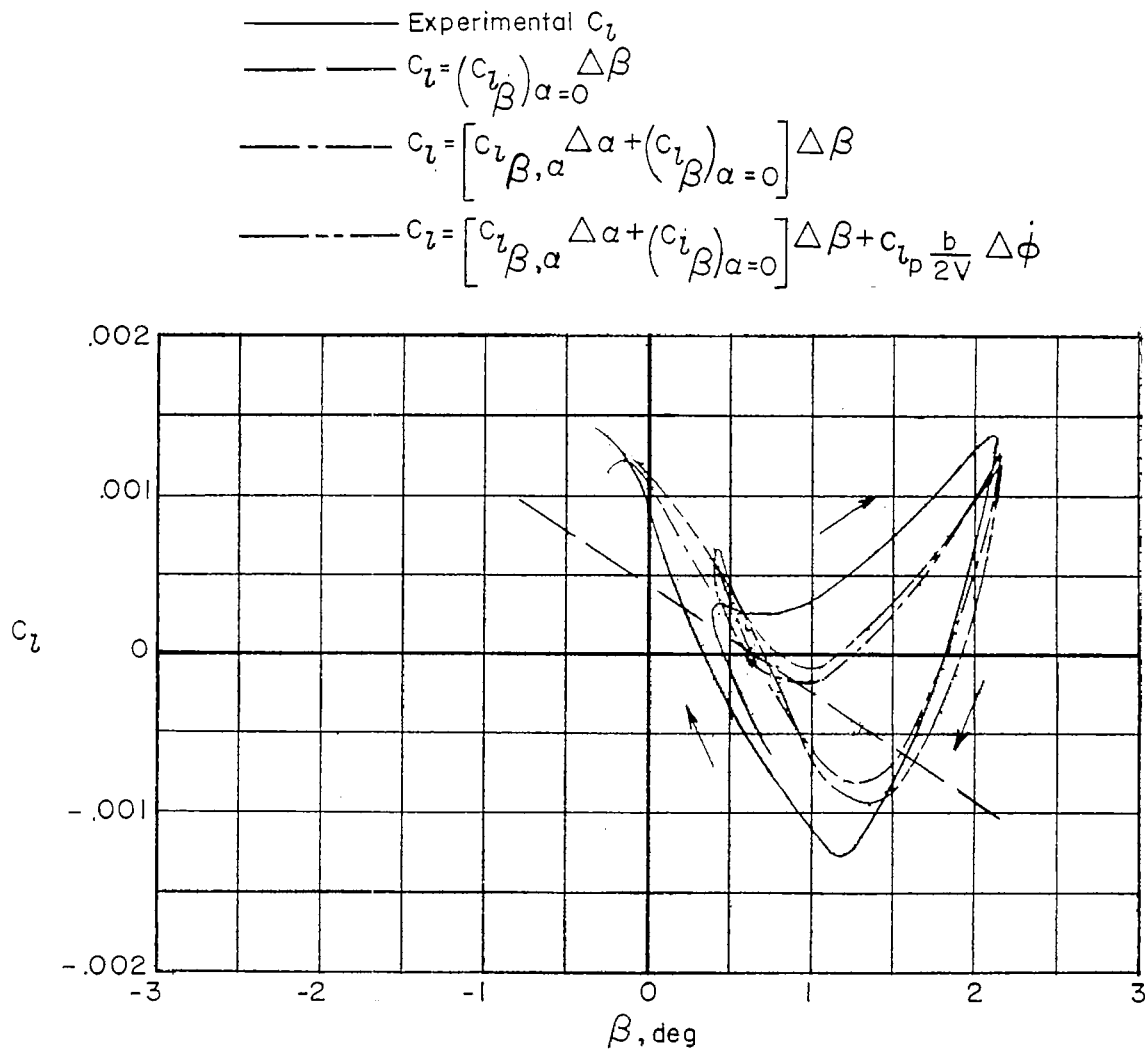(b) Rotary damping derivatives.

Figure 22.- Damping in yaw.

Figure 23.- Values of rolling-moment coefficients obtained by application of least-squares method to the rolling-moment equation.

———————— Experimental C_l

—— —— $C_l = \left(C_{l_\beta}\right)_{\alpha=0} \Delta\beta$

—— · —— $C_l = \left[C_{l_{\beta,\alpha}} \Delta\alpha + \left(C_{l_\beta}\right)_{\alpha=0}\right] \Delta\beta$

—— ·· —— $C_l = \left[C_{l_{\beta,\alpha}} \Delta\alpha + \left(C_{l_\beta}\right)_{\alpha=0}\right] \Delta\beta + C_{l_p} \frac{b}{2V} \Delta\dot{\phi}$
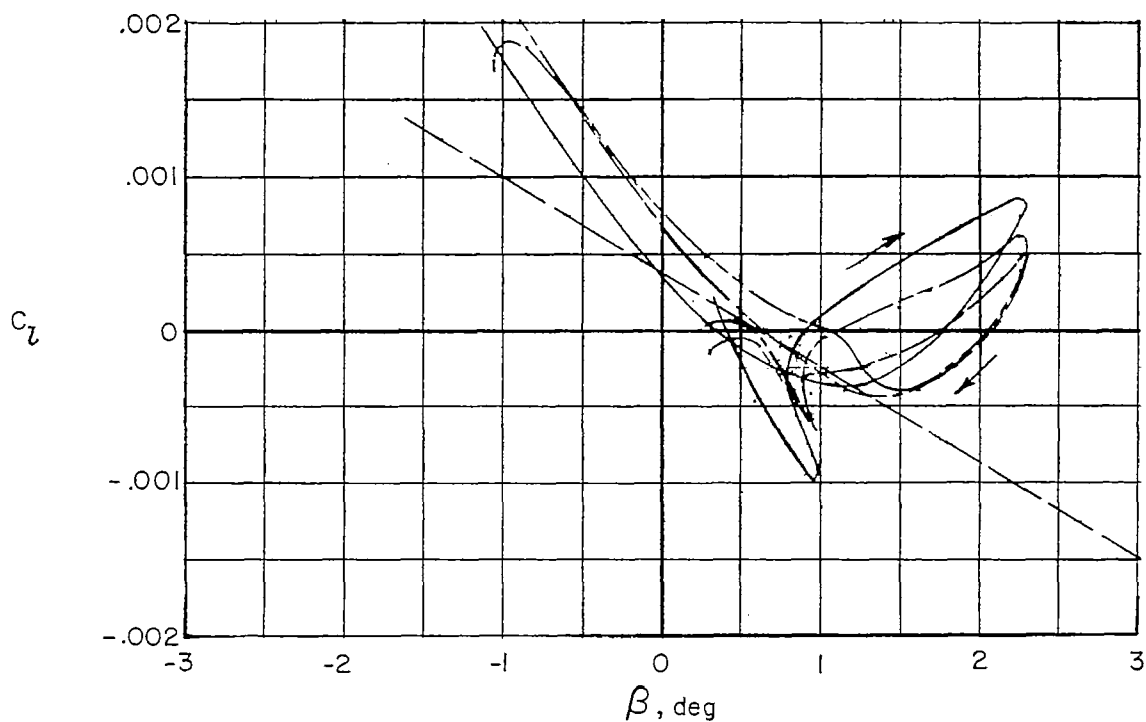

(a) Mach number, 1.25.

Figure 24.- Comparison of experimental and calculated rolling-moment-coefficient variation with sideslip angle. Model pulsed in pitch.
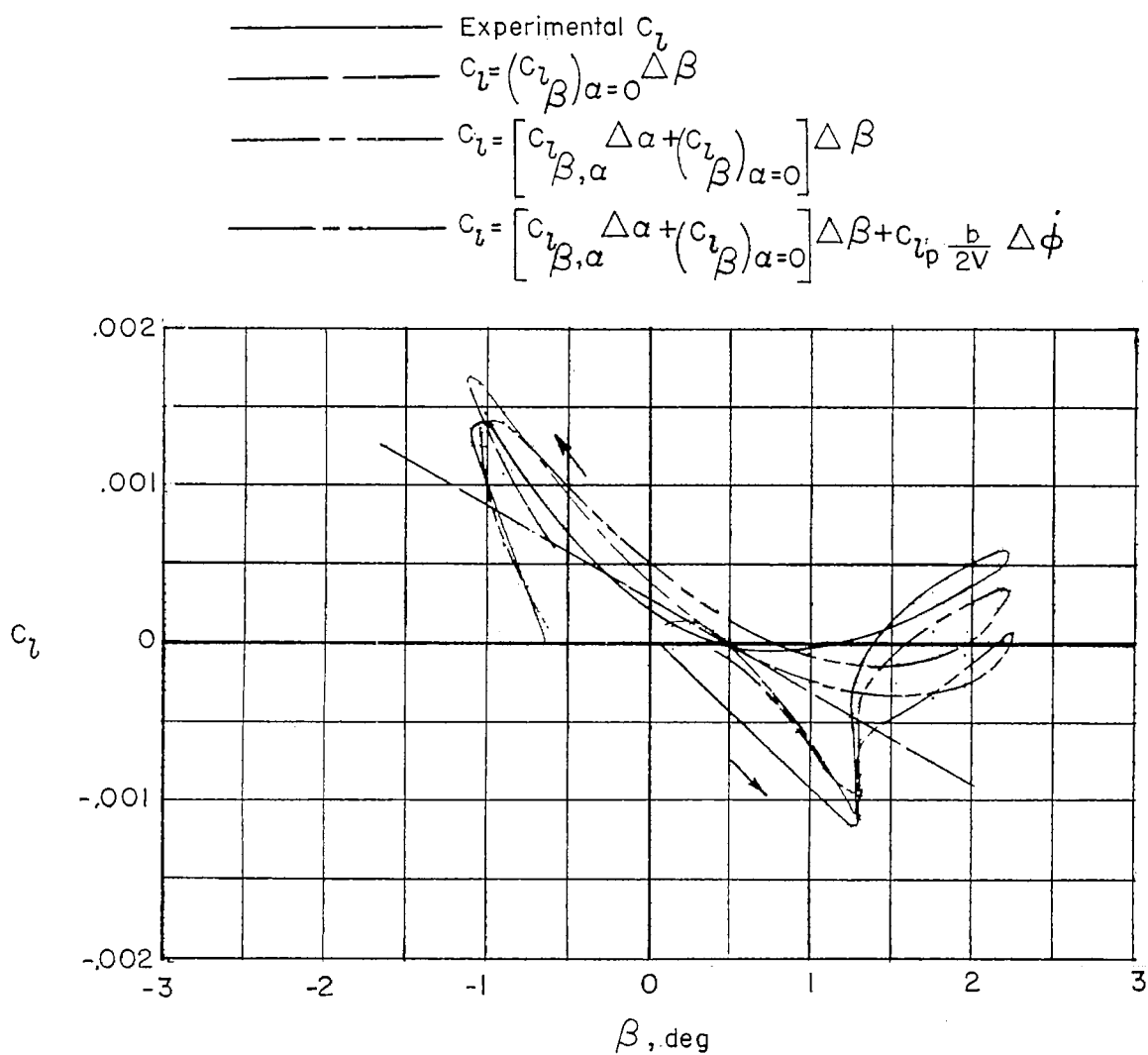
——————— Experimental C_l

——— ——— $C_l = \left(C_{l_\beta}\right)_{\alpha=0} \Delta\beta$

——— · ——— $C_l = \left[C_{l_{\beta,\alpha}} \Delta\alpha + \left(C_{l_\beta}\right)_{\alpha=0}\right] \Delta\beta$

——— ·· ——— $C_l = \left[C_{l_{\beta,\alpha}} \Delta\alpha + \left(C_{l_\beta}\right)_{\alpha=0}\right] \Delta\beta + C_{l_p} \dfrac{b}{2V} \Delta\dot\phi$

(b) Mach number, 1.46.

Figure 24.- Continued.

Experimental C_l

$C_l = \left(C_{l_\beta}\right)_{\alpha=0} \Delta\beta$

$C_l = \left[C_{l_{\beta,\alpha}} \Delta\alpha + \left(C_{l_\beta}\right)_{\alpha=0}\right]\Delta\beta$

$C_l = \left[C_{l_{\beta,\alpha}} \Delta\alpha + \left(C_{l_\beta}\right)_{\alpha=0}\right]\Delta\beta + C_{l_p}\frac{b}{2V}\,\Delta\dot{\phi}$

(c) Mach number, 1.69.

Figure 24.- Continued.

$$\text{---------} \quad \text{Experimental } C_l$$

$$\text{--- --- ---} \quad C_l = \left(C_{l_\beta} \right)_{\alpha=0} \Delta\beta$$

$$\text{--- --- ---} \quad C_l = \left[C_{l_{\beta,\alpha}} \Delta\alpha + \left(C_{l_\beta} \right)_{\alpha=0} \right] \Delta\beta$$

$$\text{--- --- ---} \quad C_l = \left[C_{l_{\beta,\alpha}} \Delta\alpha + \left(C_{l_\beta} \right)_{\alpha=0} \right] \Delta\beta + C_{l_p} \frac{b}{2V} \Delta\phi$$
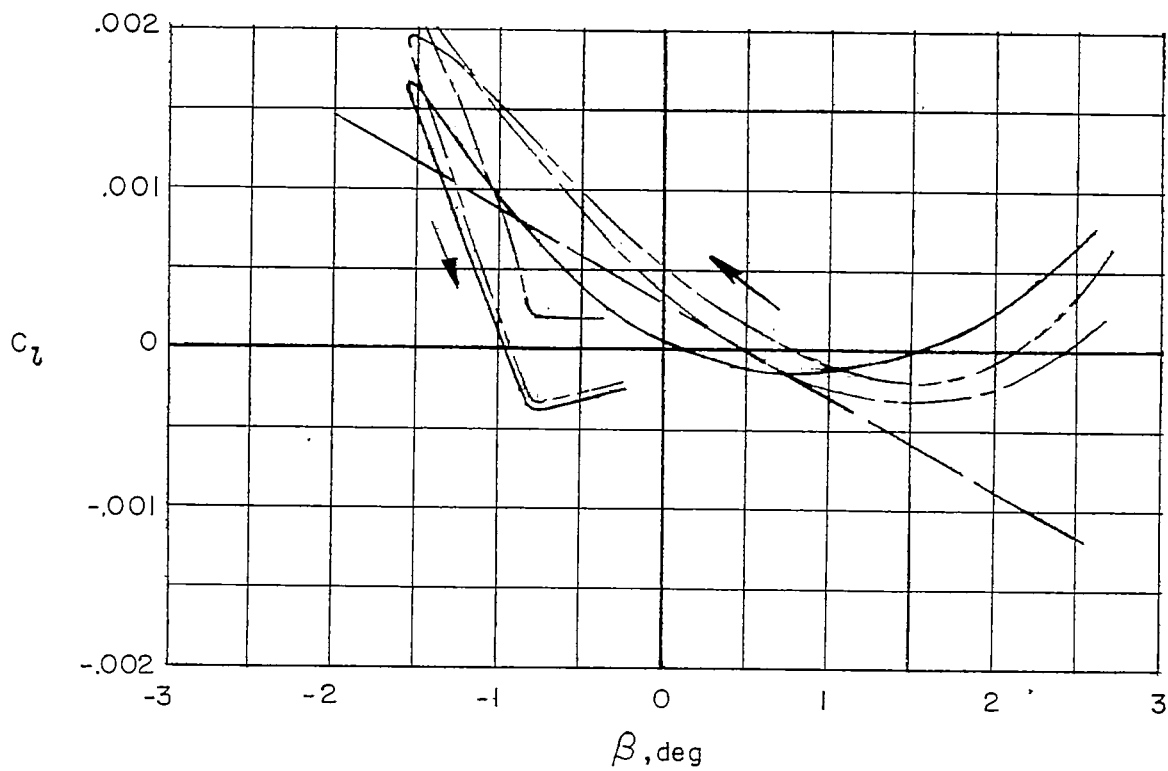
(d) Mach number, 1.81.

Figure 24.- Concluded.

$$C_l = \left(C_{l_\beta}\right)_{\alpha=0} \Delta\beta$$
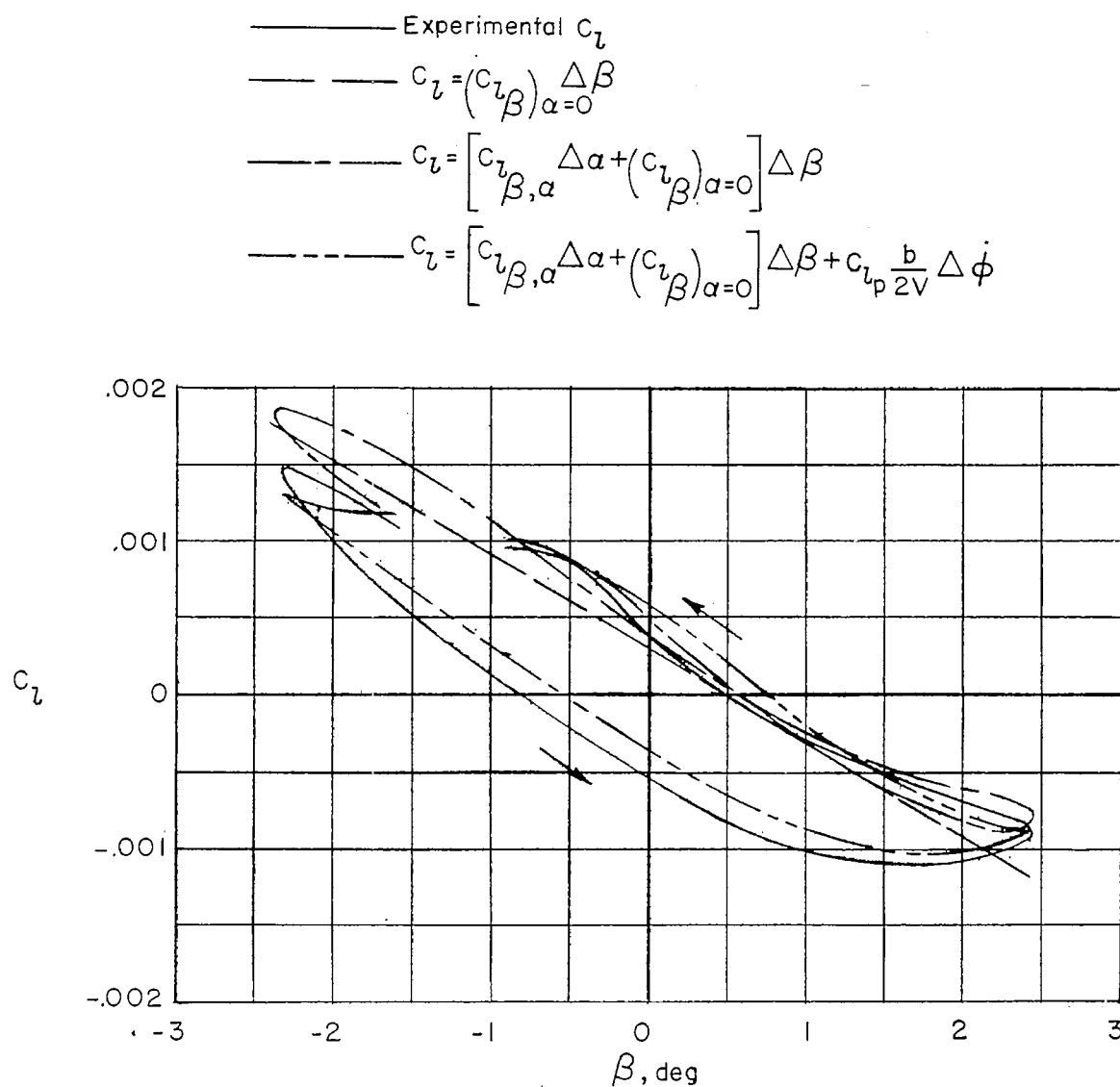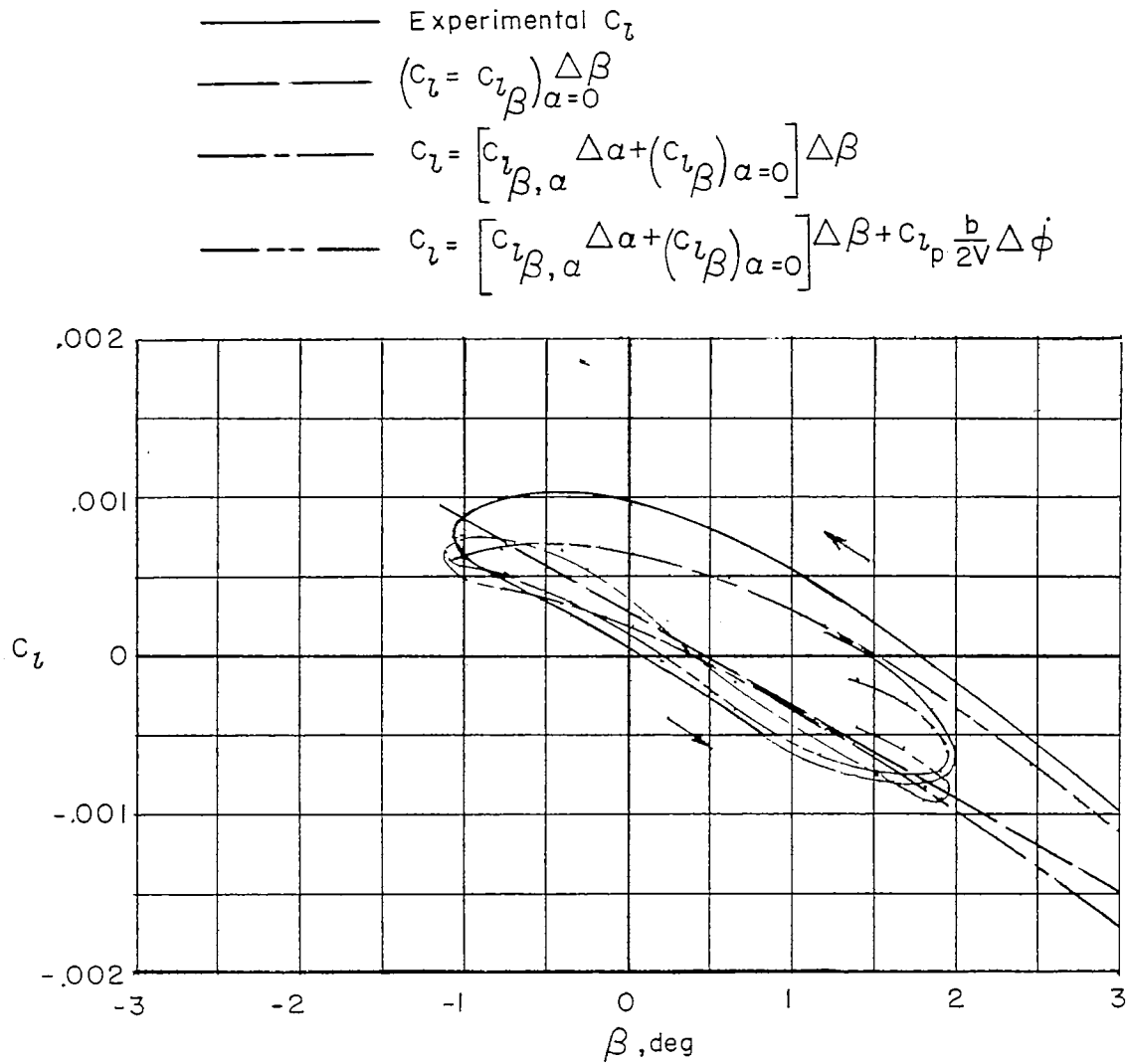
(a) Mach number, 1.59.

Figure 25.- Comparison of experimental and calculated rolling-moment-coefficient variation with sideslip angle. Model pulsed in yaw.

$$\text{Experimental } C_l$$

$$\left(C_l = C_{l_\beta}\right)_{\alpha=0} \triangle\beta$$

$$C_l = \left[C_{l_{\beta,\alpha}} \triangle\alpha + \left(C_{l_\beta}\right)_{\alpha=0}\right]\triangle\beta$$

$$C_l = \left[C_{l_{\beta,\alpha}} \triangle\alpha + \left(C_{l_\beta}\right)_{\alpha=0}\right]\triangle\beta + C_{l_p}\frac{b}{2V}\triangle\dot\phi$$

(b) Mach number, 1.86.

Figure 25.- Concluded.